Title: Fast inhibition slows and desynchronizes mouse auditory efferent neuron activity

Authors

Matthew Fischl[1,2], Alia Pederson[1,3], Rebecca Voglewede[1], Hui Cheng[4], Jordan Drew[1,5], Lester Torres Cadenas[1], and Catherine J.C. Weisz[1*]

Author Affiliations:

[1]Section on Neuronal Circuitry, National Institute on Deafness and Other Communication Disorders, NIH, Bethesda, MD 20892, USA

[2]Current affiliation: Lafayette College, Neuroscience Program, Easton, PA 18042, USA

[3]Current affiliation: The University of Texas at Austin Dell Medical School, Austin, TX 78712, USA

[4]Bioinformatics and Biostatistics Collaboration Core, National Institute on Deafness and Other Communication Disorders, NIH, Bethesda, MD 20892, USA

[5]Current affiliation: Institute for Learning and Brain Sciences, University of Washington, Seattle, WA, 98195, USA

[*]Corresponding Author: Catherine J.C. Weisz, Section on Neuronal Circuitry, National Institutes of Health, National Institute on Deafness and Other Communication Disorders. 35A Convent Drive Room 3E450, Bethesda, MD 20892, USA. Email: catherine.weisz@nih.gov

Preprint Server: This manuscript was submitted to BioRXiv: https://doi.org/10.1101/2023.12.21.572886. The copyright holder for this preprint is the author/funder, who has granted bioRxiv a license to display the preprint in perpetuity. This article is a US Government work. It is not subject to copyright under 17 USC 105 and is also made available for use under a CC0 license.

Conflicts of Interest: The authors declare no competing financial interests.

Classification: Biological Sciences, Neuroscience

Keywords: auditory, efferent, olivocochlear, MNTB, inhibition, cochlear nucleus, globular bushy cell, T-stellate cell

Fast inhibition slows and desynchronizes mouse auditory efferent neuron activity

Abstract

The encoding of acoustic stimuli requires precise neuron timing. Auditory neurons in the cochlear nucleus (CN) and brainstem are well-suited for accurate analysis of fast acoustic signals, given their physiological specializations of fast membrane time constants, fast axonal conduction, and reliable synaptic transmission. The medial olivocochlear (MOC) neurons that provide efferent inhibition of the cochlea reside in the ventral brainstem and participate in these fast neural circuits. However, their modulation of cochlear function occurs over time scales of a slower nature. This suggests the presence of mechanisms that restrict MOC inhibition of cochlear function. To determine how monaural excitatory and inhibitory synaptic inputs integrate to affect the timing of MOC neuron activity, we developed a novel in vitro slice preparation ('wedge-slice'). The wedge-slice maintains the ascending auditory nerve root, the entire CN and projecting axons, while preserving the ability to perform visually guided patch-clamp electrophysiology recordings from genetically identified MOC neurons. The 'in vivo-like' timing of the wedge-slice demonstrates that the inhibitory pathway accelerates relative to the excitatory pathway when the ascending circuit is intact, and the CN portion of the inhibitory circuit is precise enough to compensate for reduced precision in later synapses. When combined with machine learning PSC analysis and computational modeling, we demonstrate a larger suppression of MOC neuron activity when the inhibition occurs with in vivo-like timing. This delay of MOC activity may ensure that the MOC system is only engaged by sustained background sounds, preventing a maladaptive hyper-suppression of cochlear activity.

Significance Statement

Auditory brainstem neurons are specialized for speed and fidelity to encode rapid features of sound. Extremely fast inhibition contributes to precise brainstem sound encoding. This circuit also projects to medial olivocochlear (MOC) efferent neurons that suppress cochlear function to enhance detection of signals in background sound. Using a novel brain slice preparation with intact ascending circuitry, we show that inhibition of MOC neurons can also be extremely fast, with the speed of the circuit localized to the cochlear nucleus. In contrast with the enhancement of precision afforded by fast inhibition in other brainstem auditory circuits, inhibition to MOC neurons instead

has a variable onset that delays and desynchronizes activity, thus reducing precision for a slow, sustained response to background sounds.

Introduction

The encoding of acoustic stimuli is enhanced and sharpened by active cochlear processes termed 'cochlear amplification', including electromotility of outer hair cells (OHC)[1–4]. Medial olivocochlear (MOC) neurons provide efferent feedback to the OHCs to inhibit this electromotility[5–10]. The subsequent suppression of sound-evoked basilar membrane vibrations improves detection of salient sounds in background noise, provides protection from noise-evoked damage, and may contribute to auditory attention[11–16]. While the impact of the cholinergic MOC synapses onto OHCs is well-characterized at the synaptic output level, the synaptic inputs onto MOC neurons in the ventral nucleus of the trapezoid body (VNTB) within the superior olivary complex (SOC) are incompletely characterized. Recent work in positively identified MOC neurons in brain slices from transgenic mice has demonstrated that cochlear nucleus (CN) T-stellate cells provide ascending afferent excitation, along with descending excitation from the inferior colliculus (IC)[17]. MOC neurons also receive afferent inhibition from the medial nucleus of the trapezoid body (MNTB) which can delay spontaneous APs in vitro[18], and may prevent MOC neuron suppression of rapidly changing auditory stimuli[19]. MOC neuron properties allow for high frequency APs (>300 Hz) in vitro[17,20,21]. However, in vivo, MOC neurons rarely fire APs faster than 100 Hz even with high intensity sound stimulation[22–25], and have variable latencies to APs[23,24,26]. These results indicate that MOC neurons do not operate as a simple reflex that is immediately active in response to excitatory drive from the CN. Rather, a combination of excitatory, inhibitory, and modulatory inputs may shape MOC activity in changing sound conditions.

The ascending auditory pathways from the cochlea through the brainstem have electrical and morphological specializations for temporal precision and fidelity. In particular, the three-neuron pathway (AN–GBC–MNTB) that provides the primary inhibitory synapses throughout the SOC are among the fastest, most powerful, high-fidelity circuits in the brain[27–30], although mice have fewer GBC specializations compared to other species[31]. It is unknown whether the MNTB–GBC pathway projections to MOC neurons are also exceptionally fast, or how the timing of inhibition affects MOC neuron function.

Brain slice preparations used for synaptic physiology studies allow extensive pharmacological manipulations of circuitry, but often sever long-distance or circuitous projections, thus losing the cellular interactions that govern the timing, strength, and plasticity of incoming neuron pathways. Therefore, we developed a novel asymmetric slice preparation, the 'wedge-slice', that maintains sound-evoked monaural ascending circuitry[32]. This preparation enables investigation into how integration of ascending excitation and inhibition affects MOC neuron function. On one side, the slice is thin enough to allow the light penetration needed for visualization during typical whole-cell patch clamp electrophysiology experiments from MOC neurons. On the other (contralateral) side, where primary excitatory and inhibitory auditory inputs originate, the slice is thicker. This maintains the auditory nerve root as it enters the CN, the full circuitry of the CN, and the primary excitatory (direct) and inhibitory (via MNTB) axon projections from the CN to the VNTB where MOC neuron recordings are performed.

We compared the synaptic inputs to MOC neurons when stimulated at the midline (MdL) to bypass intrinsic CN circuitry vs stimulating the auditory nerve (AN) root to engage the full complement of CN circuits. We found that GBC-MNTB projections to MOC neurons are exceptionally fast and temporally precise, similar to projections to other auditory nuclei. Both the speed and precision of the circuit can be attributed to GBC neurons compensating for reduced precision in later synapses and highlighting the 'coincidence detector' function of GBCs[33–35]. A computational model of MOC neurons demonstrated that the enhanced speed of the AN–GBC–MNTB–MOC inhibitory pathway as measured during in vivo-like wedge-slice conditions has a larger effect on suppressing activity in MOC neurons compared to with simple stimulation (MdL-stimulation). This increased speed of inhibition delayed AP onset in MOC neurons, while variability of inhibitory timing across the population of MOC neurons results in stochastic activity that may provide smooth inhibition of cochlear function.

Results

<u>Midline stimulation in wedge-slice preparations evokes mixed excitatory and inhibitory post-synaptic currents (PSCs)</u>

Ascending axons conveying acoustic information from the CN throughout the SOC traverse near the ventral surface of the brainstem. This includes axons projecting to MOC neurons in the VNTB that provide sound-evoked excitation, primarily T-stellate and possibly small cell

124 cap (SCC) neurons[17,36–39]. This also includes axons of GBCs which provide sound-evoked
125 inhibition via intervening MNTB neurons[18]. To investigate the convergence of these pathways,
126 whole cell patch-clamp recordings were performed in voltage-clamp from positively identified
127 MOC neurons in brainstem slices from postnatal day fourteen through nineteen (P14-P19) ChAT-
128 IRES-Cre; tdTomato mice of both sexes. We used a combination of uniformly thick (300 micron)
129 slices cut at ~15 degrees off the coronal plane[18] and wedge-slices[32] (**Figure 1A**) while electrically
130 stimulating close to the ventral surface of the slice near the midline (MdL) to evoke
131 neurotransmitter release from pre-synaptic axons. These axons likely originated in the CN
132 contralateral to the MOC neuron. With this technique, both excitatory and inhibitory circuits
133 originating at the contralateral CN can be simultaneously stimulated. MdL-stimulation in this
134 location is expected to directly activate T-stellate cell axons resulting in mono-synaptically
135 evoked, short latency excitatory post-synaptic currents (Midline-evoked EPSCs: MdL-EPSCs).
136 Additionally, stimulation of GBC axons accessed from the same location results in inhibitory post-
137 synaptic currents (Midline-evoked IPSCs: MdL-IPSCs) evoked via the di-synaptic GBC–MNTB-
138 MOC pathway that inhibits MOC neurons[18]. Other as-yet uncharacterized synaptic inputs to MOC
139 neurons may also be activated with this technique. Consistent with activation of multiple classes
140 of pre-synaptic axons, MdL-stimulation resulted in multi-component PSCs in 13/21 recordings
141 (**Figure 1B**). PSCs occurred with a short latency from stimulation (1.85±0.53 ms, n=557 PSCs in
142 21 neurons; a subset of PSC latency data was previously published[32]).
143 With the high intracellular chloride concentration used in voltage-clamp recordings to
144 maximize detection of IPSCs (intracellular chloride concentration = 60 mM, E_{Cl} ~-20 mV), both
145 'excitatory' and 'inhibitory' PSCs were inward at a membrane holding potential of -60 mV, and
146 therefore indistinguishable based on polarity. To distinguish between MdL-EPSCs and MdL-
147 IPSCs, in all cells the MOC neuron holding potential was alternatively set to the AMPA receptor
148 reversal potential of 0 mV to isolate outward, chloride-mediated PSCs that can be classified as
149 'inhibitory' that are likely either GABAergic or glycinergic. In each experiment, stimulation was
150 performed repeatedly (20-80 stimulations; **Figure 1B**), and in each sweep, PSCs were detected
151 and analyzed for parameters of onset latency, rise time (10-90% of peak), amplitude, and time
152 constant of decay. These parameters (excluding amplitude) were used to sort PSCs into statistically
153 defined clusters using k-means analyses (Methods). Clusters observed at both –60 mV and 0 mV
154 holding potentials were classified as 'inhibitory' MdL-IPSCs and clusters observed only at –60

155 mV were classified as 'excitatory' MdL-EPSCs (**Figure 1C**, each peak indicates a different
156 'cluster').

157 Following classification of PSCs as 'excitatory' or 'inhibitory' based on the presence or
158 absence of the PSC cluster at a holding potential of 0 mV, we further characterized MdL-PSCs
159 recorded at -60 mV. Latency to the first MdL-EPSC was shorter than the latency to the first MdL-
160 IPSC (p=4.79E-06). MdL-EPSCs and MdL-IPSCs had similar amplitudes at -60 mV (p=0.69).
161 MdL-EPSCs had faster kinetics than MdL-IPSCs (rise time: p=8.02E-04, time constant of decay:
162 p=4.95E-07, **Table S1, Figure 1D**), consistent with earlier work[18]. Patterns of PSCs varied
163 somewhat across MdL stimulation experiments. Patterns included recordings with EPSCs only
164 (6/21), IPSCs only (4/21), a single group of EPSCs and a single group of IPSCs (5/21 recordings),
165 and more complex patterns of EPSCs and IPSCs (6/21) (**Figure 1C**). In all recordings with both
166 EPSCs and IPSCs (11/21), EPSCs always occurred with a shorter latency than IPSCs. This shorter
167 latency was expected given that the MdL-EPSC pathway is mono-synaptic (T-stellate-MOC) while
168 the MdL-IPSC pathway is di-synaptic (GBC-MNTB-MOC), consistent with an extra synapse in
169 the MdL-IPSC pathway incurring a delay.

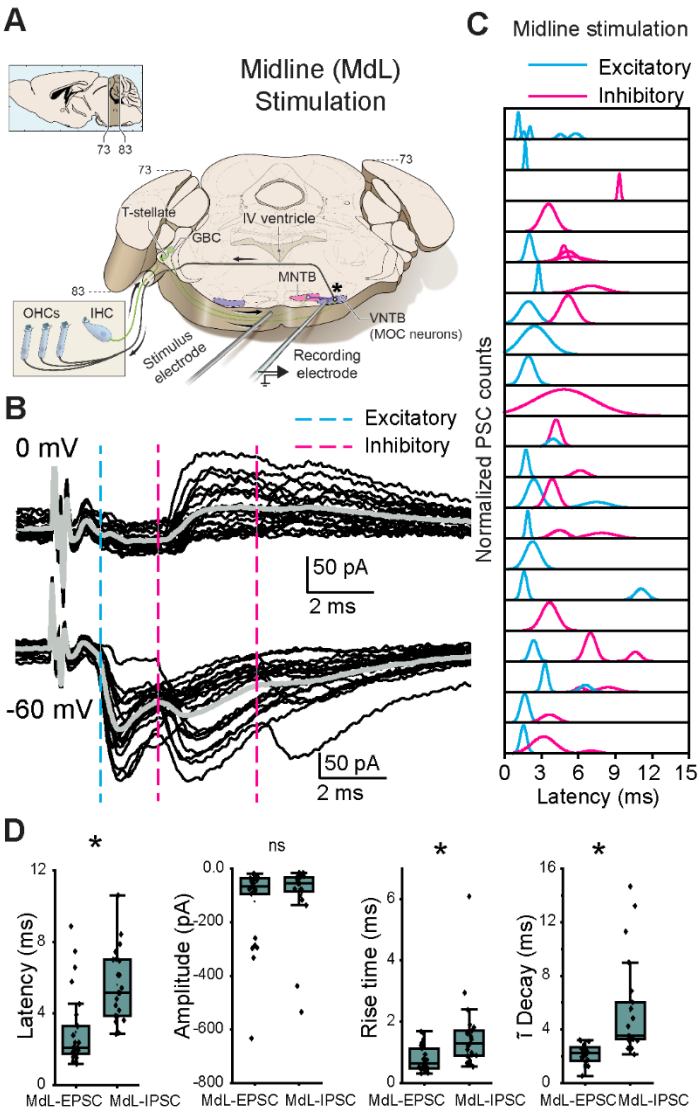

Figure 1. Stimulation of axons at the midline of the ventral brainstem evokes multi-component PSCs in MOC neurons. A. Schematic of wedge-slice preparation showing monaural circuitry of MOC neurons from ascending AN axons from the cochlea into the CN, excitatory (green) T-stellate and GBC projections to the SOC, inhibitory (purple) projections from the MNTB to the VNTB containing MOC neurons, and MOC axons (black) projecting back to cochlear OHCs. Note: the cochlea is not present in the recording preparation. Upper left schematic indicates atlas coordinates of position along rostral-caudal extent of thick portion of the slice[125]. B. Voltage-clamp traces from an identified MOC neuron during MdL-stimulation (1 Hz), evoking PSCs in multiple clusters at a holding potential of 0 mV (top) and -60 mV (bottom). 20 sweeps overlaid (black), with grey line indicating the average waveform. Dashed lines indicate the approximate onset of PSCs in clusters of excitatory (blue) and inhibitory (magenta) PSCs. C. Gaussian distributions fitted to frequency histograms (normalized) of the latency to PSC onset for clusters of MdL-EPSCs (blue), and MdL-IPSCs (magenta). Each row represents PSCs recorded in a different MOC neuron. D. Comparison of parameters observed in MdL-EPSCs and MdL-IPSCs.

186

187 Auditory nerve stimulation-evoked PSCs

188 The above experiments detail the relative timing of synaptic inputs to MOC neurons
189 evoked simultaneously at the MdL from mono-synaptic excitatory and di-synaptic inhibitory
190 inputs. The timing of synaptic inputs in above experiments with MdL-stimulation is artificial
191 because the full complexity of ascending circuitry is not activated in this stimulation paradigm,
192 including AN synapses onto CN neurons, intrinsic CN circuits, and the potential differential
193 propagation of APs down the specialized CN axons. To test the integration of ascending, monaural,
194 excitatory, and inhibitory synaptic inputs to MOC neurons with a more in vivo-like timing, PSCs
195 were evoked in MOC neurons by stimulating the contralateral AN root in wedge-slice preparations
196 (**Figure 2A**), which have an intact CN.

197 To ensure that electrical stimulation indeed excited CN neurons via synaptic activation,
198 and not direct electrical activation which would bypass the strength and timing of AN–CN
199 synapses, we performed 2-photon calcium imaging of bushy cells in wedge-slices from
200 Atoh7/Math5^{Cre} mice[40,41] expressing GCaMP6f[42] in bushy cells, to measure supra-threshold
201 activation during AN-stimulation. AN axons were stimulated in control conditions and with bath
202 application of glutamate receptor antagonists to block synaptic transmission at AN–CN synapses.
203 If the AN electrical activation stimulates glutamate release from AN axons to synaptically activate
204 bushy cells, blockade of the glutamate receptors is expected to reduce the somatic calcium
205 response. However, if AN electrical stimulation directly evokes APs in bushy cells, the calcium
206 response would be insensitive to glutamate receptor blockers.

207 AN-stimulation-evoked calcium responses were quantified for 388 neurons in 14 fields of
208 view from 8 animals (**Figure 2B,E**). Of these neurons, 227 were classified as 'active' in the control
209 condition. AN-evoked calcium responses in active bushy cells were significantly reduced by bath
210 application of the AMPA receptor antagonist CNQX (p=1.04E-20) or the combination of CNQX
211 and the NMDA receptor antagonist APV (p=1.14E-34). Calcium responses significantly recovered
212 upon wash of glutamate receptor blockers (CNQX recovery: p=2.74E-13; CNQX+APV recovery:
213 p=2.54E-24). There was a small but significant difference in the ΔF/F values between the CNQX
214 and the CNQX+APV groups (p=0.005) (**Figure 2B-D**), confirming active NMDA receptors in
215 bushy cells[43]. We explored this difference further by calculating a % suppression for each of the
216 neurons. CNQX suppressed the calcium signal by ~68% while the cocktail of CNQX+APV

suppressed the signal by ~75% (p=0.004) (**Table S2, Figure 2F**). Across cells, calcium suppression with CNQX and APV was significant but not quite complete, perhaps due to incomplete penetration of antagonists into the thick wedge-slice. However, it is notable that GBCs have a particularly small somatic AP[44–46] and an abundance of calcium permeable glutamate receptors[43]. Therefore, the relative contribution of the AP-evoked calcium signal to the total evoked calcium signal may be small, resulting in a relatively large residual calcium signal in the case of incomplete glutamate receptor block even if APs are suppressed. However, the sensitivity of calcium responses in bushy cells to glutamate receptor blockers suggests that AN-stimulation is likely activating CN neurons via synaptic, and not direct electrical excitation, maintaining the AN-CN synapses in the wedge-slice circuit for a more in vivo-like network activation.

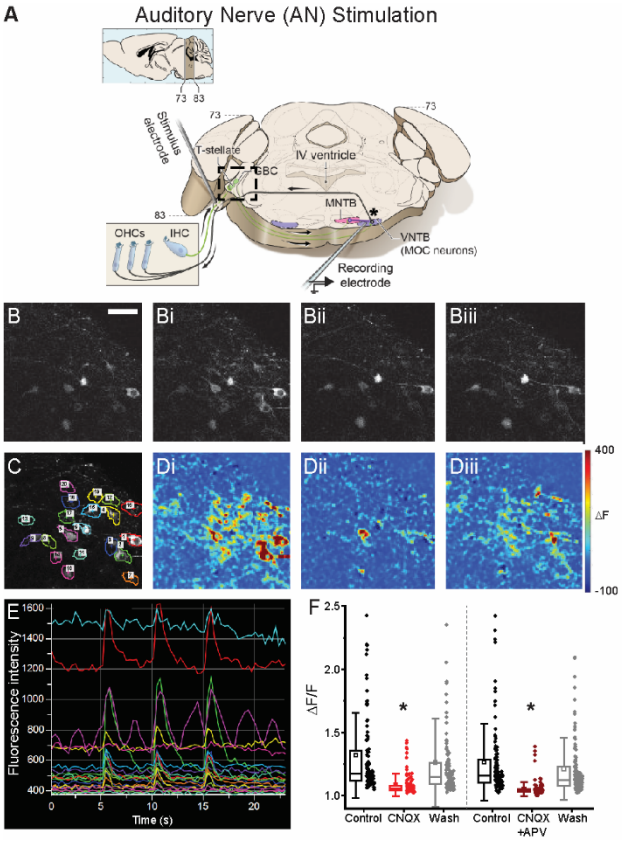

Figure 2. AN-stimulation in a wedge-slice evokes activity via synaptic activation of CN neurons. A Schematic of a wedge-slice, as in Figure 1, with stimulation at the auditory nerve root (AN-stimulation). Note: the cochlea is not present in the preparation. B. Calcium imaging of bushy cells in Atoh7/Math5^{Cre}; GCaMP6f mice during AN-stimulation in: B. Baseline (no stimulation), Bi. control AN-stimulation at 100 Hz, 20 pulses, Bii. AN-stimulation with blockers of AMPA and NMDA receptors (5 µM CNQX, 50 µM APV) in the aCSF. Biii. AN-stimulation after wash of AMPA and NMDA receptor blockers. C. Same CN imaging region as in B, annotated with ROI's

236 over individual bushy cells used for fluorescence analysis. D. Heat maps showing change in
237 fluorescence in same region as B and C during AN-stimulation, color scale indicates fluorescence
238 change from baseline in: Di. control, Dii. AMPA and NMDA block, and Diii. wash. E. Raw
239 fluorescence intensity changes for ROIs in C during 3 'bouts' (bout: 20 pulses, 100 Hz) of AN-
240 stimulation in control conditions. F. Quantification of fluorescence changes of bushy cells in
241 response to AN-stimulation in control, glutamate receptor blockade (CNQX or CNQX + APV)
242 and wash. Scale bar in B (50 μm) applies to all panels in B-D.
243

244 Multi-component synaptic responses evoked by AN-stimulation

245 To test how the extensive intrinsic circuitry of the intact CN and specialized axons
246 projecting to the SOC change the relative timing of excitatory and inhibitory synaptic inputs to
247 MOC neurons, the AN was electrically stimulated in a wedge-slice while PSCs were recorded in
248 contralateral MOC neurons (**Figure 3A**). Electrical stimulation at the AN root evoked PSCs in 11
249 of 43 MOC recordings. Similar to MdL-evoked PSCs, AN-evoked PSCs at a membrane holding
250 potential of -60 mV occurred in multi-component PSC patterns (**Figure 3B**). Overall, the latency
251 to the first PSC was significantly longer in AN- vs MdL-evoked PSCs (AN-PSC latency:
252 5.51±1.00 ms, n=11 cells; MdL-PSC latency: 1.99±0.45 ms, n=21 cells, Mann-Whitney U test
253 p=2.29E-5), consistent with an increased total number of intervening synapses causing a longer
254 synaptic delay.

255 In two experiments, AN-stimulation protocols were repeated with high intensity electrical
256 stimulation (>2000 μA), to cause greater current spread in the tissue and intentionally bypass the
257 AN–CN synapse. The high stimulation intensity significantly decreased PSC latency (AN-high
258 stim level latency: 1.65±0.1 ms, n=18 PSCs; AN-intermediate stim level latency: 4.58±0.3 ms,
259 n=27 PSCs; n=2 neurons, Mann-Whitney U test p=1.90E-8; **Figure 3C, Figure 4Fi**). This
260 indicates that with intentionally high stimulation intensity CN axons projecting to MOC neurons
261 were directly stimulated, bypassing intrinsic circuitry of the CN. Remaining experiments used the
262 lower stimulation intensity that synaptically engages, not electrically bypasses, the full
263 complement of CN circuits.

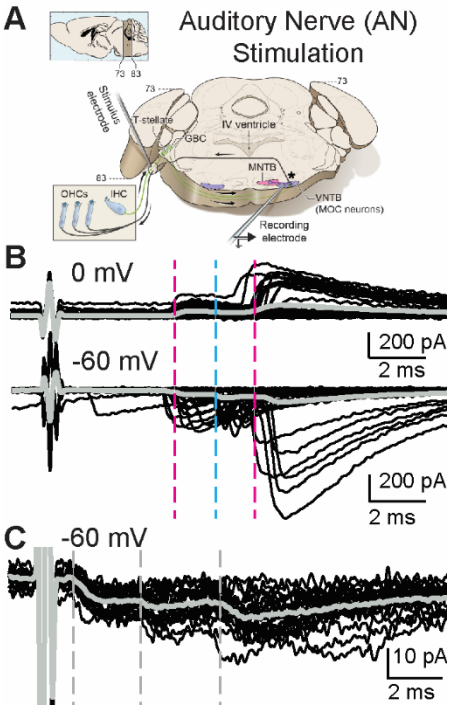

Figure 3. AN-stimulation evokes excitatory and inhibitory PSCs in MOC neurons. A. Schematic of the wedge-slice, indicating electrical stimulation of AN axons (AN-stimulation) projecting to the CN. B. Voltage-clamp traces from identified MOC neurons during AN-stimulation at 1Hz, 0 mV (top) and -60 mV (bottom). Black traces are 50 overlaid sweeps. Grey line indicates average trace. Dashed lines indicate approximate PSC onset latency for clusters of excitatory (blue) and inhibitory (magenta) PSCs. C. Voltage-clamp traces at -60 mV from a different MOC neuron than in (B) of PSCs evoked by AN-stimulation when the stimulus intensity is increased to levels high enough to evoke short-latency PSCs.

Machine Learning Algorithm to classify excitatory and inhibitory PSCs

Analysis of synaptic integration requires classification of synaptic responses as excitatory or inhibitory. In some (4/11) experiments with AN-stimulation the MOC neuron membrane holding potential was set to 0 mV to isolate IPSCs. Similar to MdL-stimulation recordings, IPSCs occurred in clusters that aligned with a subset of the clusters recorded at -60 mV (**Figure 3B**), indicating that both EPSCs and IPSCs are evoked in MOC neurons by AN-stimulation. However, for the cells lacking 0 mV data, we were initially unable to classify PSC clusters. Therefore, we used parameters of PSCs evoked from MdL-stimulation to develop a machine learning approach to characterize EPSCs and IPSCs, and then used this algorithm of MdL-evoked PSC characteristics to classify AN-evoked PSCs as excitatory or inhibitory. To accomplish this, first we developed a

285 RandomForest-based classification algorithm to identify EPSCs and IPSCs by training the model
286 on identified MdL-EPSCs and MdL-IPSCs recorded at -60 mV (**Figure 4A-D**).
287 Next, we used the trained RandomForest algorithm to classify AN-PSCs recorded at -60
288 mV as excitatory or inhibitory. The 344 AN-PSCs from 11 MOC neuron recordings were clustered
289 in the same manner as the MdL-PSCs (above), and the PSC parameters were calculated on a PSC-
290 by-PSC basis (rise time, time constant of decay, amplitude, animal age) or a cluster-by-cluster
291 basis (onset jitter, peak jitter, PSC probability). The AN-PSCs were then fed into the trained
292 RandomForest algorithm, which gave the probability that each AN-PSC could be classified as AN-
293 EPSC or AN-IPSC.
294
295 AN-evoked synaptic responses
296 We then determined the effect of AN-PSCs on MOC neurons. Following classification of
297 AN-EPSCs and AN-IPSCs responses at -60 mV using the RandomForest algorithm above, the
298 parameters of AN-EPSCs and AN-IPSCs for all clusters were summarized to determine their
299 effects on MOC neurons (**Table S3, Figure 4E**). AN-EPSCs and AN-IPSCs at -60 mV had similar
300 amplitudes (p=0.14) and kinetics (rise time: p=0.35, time constant of decay p=0.67). The median
301 AN-EPSC latency occurred with a significantly shorter latency than AN-IPSCs (p=0.04), but in
302 two cells AN-IPSCs occurred with shorter latencies than AN-EPSCs, similar to projections to
303 MSO neurons[28]. AN-evoked PSCs also occurred in complicated patterns that could have multiple
304 excitatory or inhibitory clusters (**Figure 4F,** each peak indicates a different 'cluster'). PSCs evoked
305 by AN-stimulation were more likely to have 'complex' patterns with two or more clusters of either
306 EPSCs or IPSCs (AN 8/11 vs MdL 8/21 complex clusters), interpreted here as PSCs from multiple
307 pre-synaptic sources.

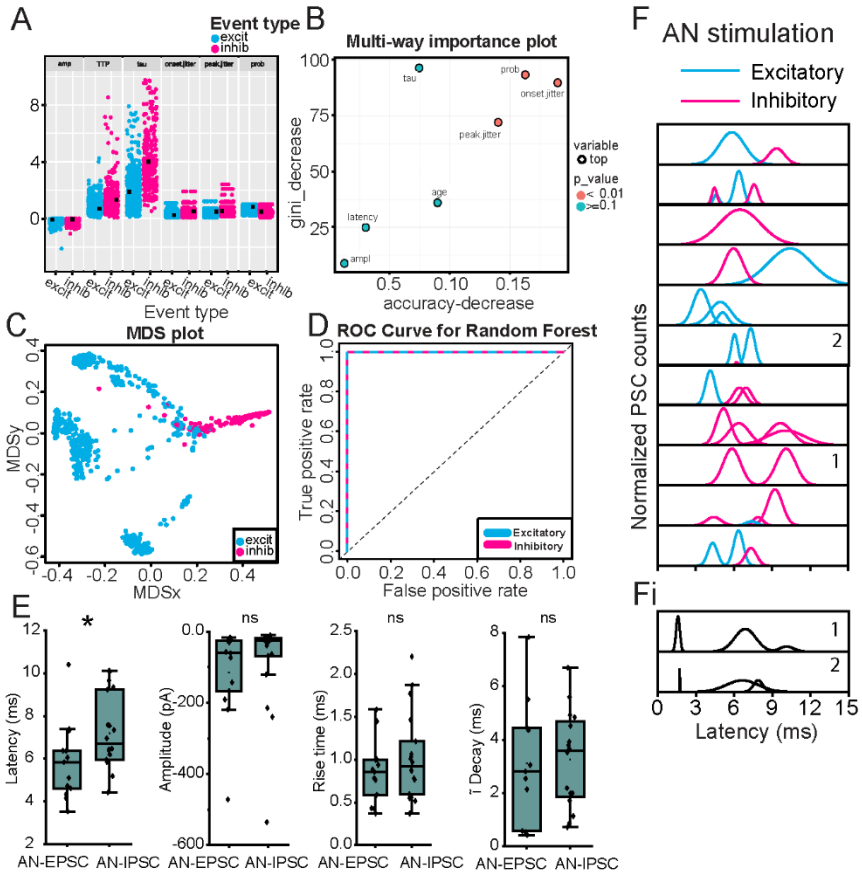

Figure 4. Multi-component PSCs evoked by AN-stimulation in a wedge-slice. A. Data points for each of seven variables (amp = amplitude; TTP = time to peak; tau = time constant of decay; prob = PSC probability) from MdL-EPSCs (blue) and MdL-IPSCs (magenta) used to train the RandomForest machine learning algorithm. B. Importance plot of variables used for RandomForest algorithm. C. Multidimensional Scaling (MDS) plot of proximity matrix showing separation of MdL-EPSCs and MdL-IPSC variables. D. ROC Curve for excitatory and inhibitory MdL-PSCs. The algorithm had a 99.89% classification accuracy. E. Comparison of parameters of AN-EPSCs and AN-IPSCs. F. Gaussian fits to frequency histograms (normalized) indicating the latency to clusters of AN-EPSCs (blue) and AN-IPSCs (magenta). Each row represents a different MOC neuron. Fi. Gaussian fits to frequency histograms (normalized) indicating the latency to clusters of AN-PSCs after the stimulation intensity was increased to higher levels that recruit short-latency PSCs. Numbers in panels in F and Fi indicate PSC clusters recorded from the same MOC neuron with intermediate (F) and high (Fi) stimulation intensities.

Comparison of PSCs evoked by MdL- vs AN-stimulation demonstrated a specialized function of CN circuitry, which was both intact and engaged during AN-stimulation but not MdL-stimulation. Above data (**Figure 4**) examines all AN-PSCs, but here we consider the first excitatory cluster and first inhibitory cluster to isolate our analyses to direct ascending pathways.

328 The overall latency to the first AN-PSCs was increased compared to MdL-PSCs, as expected
329 because AN-stimulation includes at least one more synapse (AN-CN neurons) compared to MdL-
330 stimulation. This occurred for both EPSCs and IPSCs (MdL-EPSC vs AN-EPSC latency, p=8.98E-
331 5; MdL-IPSC vs AN-IPSC latency, p=0.049). However, the additional circuitry added during AN-
332 stimulation does not alter EPSC and IPSC timing to the same degree. When comparing MdL-
333 stimulation evoked EPSCs and IPSCs, MdL-EPSCs are significantly shorter latency than MdL-
334 IPSCs (p=4.79E-6), and MdL-IPSCs are never recorded before MdL-EPSCs in any cell. In
335 contrast, when stimulating the AN, there is no significant difference in latency between AN-EPSCs
336 and AN-IPSCs (p=0.30), suggesting that the CN circuitry can compensate in speed for the
337 additional synapse present in the IPSC pathway to equalize the timing of the excitatory and
338 inhibitory pathways (**Table S4, Figure 5A**). This is also apparent when calculating the "E-I latency
339 difference" on a cell-by-cell basis, for which the latency to the first IPSC is subtracted from the
340 latency to the first EPSC. MdL-stimulated EPSCs all had positive E-I latency difference values
341 that were significantly different from zero (One-Sample Wilcoxon Signed Rank Test, p=0.0039),
342 indicating that excitation always preceded inhibition. However, the AN-stimulation E-I latency
343 difference was smaller than the MdL-stimulation E-I latency difference (MdL: 2.80±0.88, n=11
344 cells; AN: 0.14±2.87, n=7 cells, Mann-Whitney U test p=0.085), and not significantly different
345 from zero (One-Sample Wilcoxon Signed Rank Test, p=1). Further, two AN-stimulation
346 experiments had negative E-I latency differences, indicating that inhibition preceded excitation in
347 these cells. These data confirm the unusual speed of the inhibitory pathway from the CN to the
348 SOC relative to the excitatory pathway. Further, comparison of AN-stimulation and MdL-
349 stimulation synaptic timing demonstrates that the remarkable speed of the inhibitory pathway is
350 localized to components of the circuit added to the preparation during AN-stimulation, namely the
351 AN synapse onto the GBCs and the GBCs themselves.

352 Auditory brainstem circuits contain extremely precise neurons, so the timing and precision
353 of synaptic inputs evoked from MdL- vs AN-stimulation experiments was investigated to
354 determine if MOC synaptic inputs are comparably temporally precise. The onset jitter of PSCs was
355 computed for the first EPSC cluster and first IPSC cluster per MOC neuron for both MdL- and
356 AN-stimulation (**Figure 5B**). A simplistic view suggests that each additional synapse in a pathway
357 would increase the overall pathway jitter, resulting in EPSCs having less jitter than IPSCs in all
358 recording configurations. Indeed, monosynaptic T-stellate-MOC MdL-EPSCs had lower jitter than

359 di-synaptic GBC-MNTB-MOC MdL-IPSCs (p=0.015). However, AN-EPSC jitter is not different
360 from AN-IPSC jitter (p=0.30), The lack of difference in jitter between the excitatory and inhibitory
361 pathways with AN-stimulation suggests that the inhibitory pathway can compensate for having an
362 additional synapse by having enhanced precision in the CN. There was no difference in PSC
363 probability between MdL-EPSCs and MdL-IPSCs (p=0.08), and there was also no difference in
364 probability of AN-EPSCs and AN-IPSCs (p=0.16). However, when stimulating at the AN, both
365 the excitatory and inhibitory pathways have a lower probability of PSCs compared to stimulating
366 at the MdL (**Table S4, Figure 5C**). This was unexpected for the inhibitory pathway that has a high
367 proportion of suprathreshold PSPs[34,43,45], and unexpectedly indicates a reduced throughput at the
368 endbulb–GBC synapse compared to stimulating the GBC–MNTB synapse alone in our
369 experiments with MdL-stimulation.
370

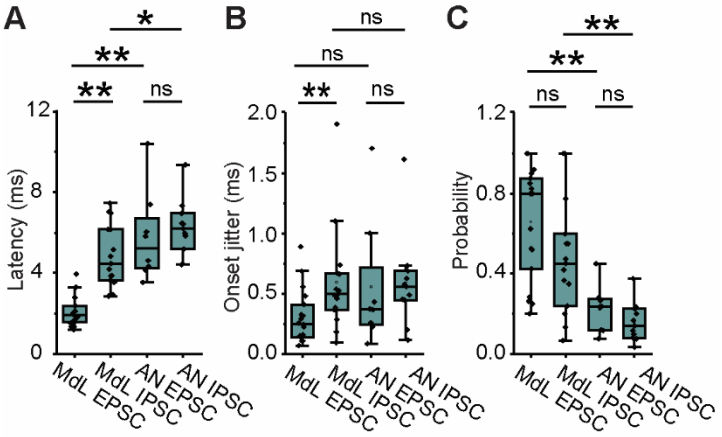

371
372

373 **Figure 5. Comparison of PSCs evoked from MdL- vs AN-stimulation.** A-C. Plot of A. Latency
374 to PSC onset, B. Synaptic jitter of PSC onset, and C. Probability of recording a PSC for MdL- vs
375 AN-EPSCs and IPSCs in the first cluster recorded in each MOC neuron.
376

377 <u>Summation of ascending MdL-evoked synaptic inputs drives APs in MOC neurons</u>

378 The voltage-clamp experiments above demonstrate that the inhibitory pathways projecting
379 to MOC neurons can be remarkably fast when the in vivo-like circuitry is intact. However, the
380 impact of the timing of inhibition on MOC neuron AP activity is unknown. We tested integration
381 under more physiological conditions of low intracellular chloride (7.2 mM, E_{Cl} = -74 mV), without
382 intracellular QX-314, and in the current-clamp configuration. We stimulated both excitatory and
383 inhibitory synaptic pathways simultaneously to record post-synaptic potentials (PSPs) and

resulting APs in MOC neurons using the MdL-stimulation configuration because these experiments were high-throughput enough to allow pharmacological blockade of inhibitory synaptic inputs. MdL-stimulation was applied in trains to evoke PSPs (MdL-PSPs) (**Figure 6A, Ai**). Summation of MdL-PSPs evoked APs, with increased stimulation rates evoking APs with an increased probability, increased rate, and reduced latency to the first AP (Friedman ANOVA: AP probability: p=0.031, AP rate: p=0.007, number of stimulations to first AP: p=0.041, Latency to first AP: p=4.6E-4; **Figure 6A, C; Table S5**).

We then tested the effect of inhibition on AP rates in MOC neurons in response to MdL-stimulation by blocking inhibitory neurotransmitter receptors. In the absence of inhibitory neurotransmission, there was an increased AP probability and rate, decreased number of stimulations to the first AP, and decreased latency to the first AP for 100 and 200 Hz stimulation rates (**Figure 6B, C; Table S5**).

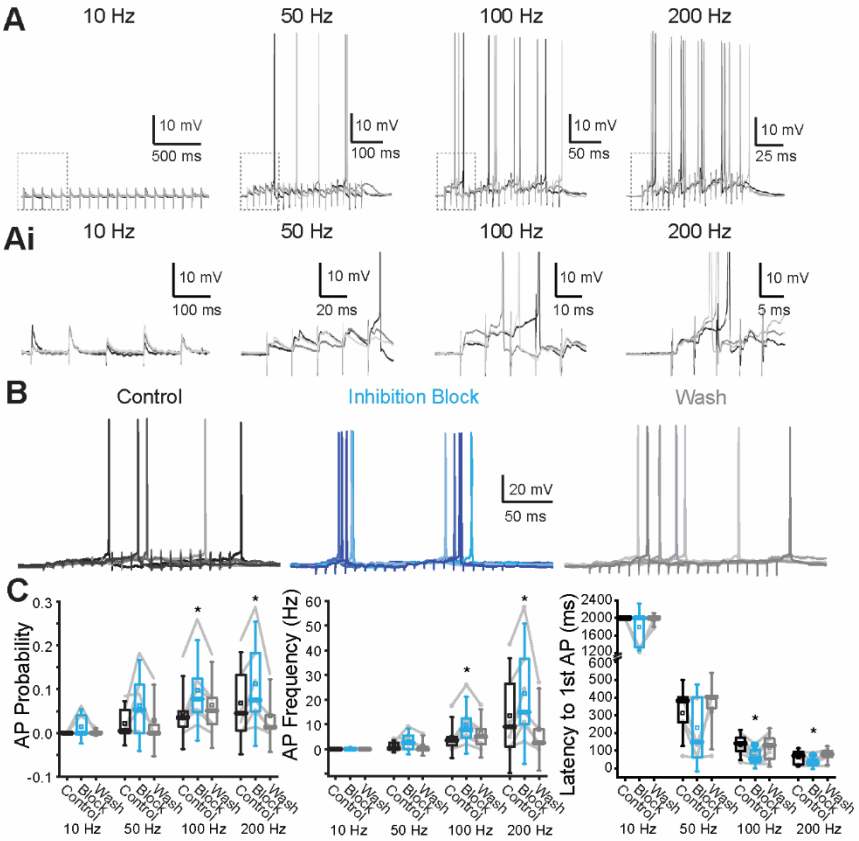

Figure 6. Inhibition reduces AP activity in MOC neuron recordings in response to MdL-PSPs. A. Current-clamp recordings from an MOC neuron while evoking MdL-PSPs for 20 pulses at 10, 50, 100, and 200 Hz. Three sweeps shown, overlaid, at each stimulation rate. Ai. Zoom of regions in each panel of (A) indicated by dashed box, showing the first five PSPs evoked in MdL-

402 stimulation trains. B. 100 Hz MdL-stimulation-evoked PSPs summate to generate AP trains in
403 control conditions (left), in the presence of 50 μM gabazine and 1 μM strychnine to block
404 inhibitory inputs ("Inhibition block", center), and after wash of inhibitory receptor blockers (right).
405 5 sweeps are overlaid per condition. C. Quantification of AP probability (left), frequency (center),
406 and latency to first AP (right) for 5-8 neurons.

407

408 Computational model of MOC neurons to assess integration of excitation and inhibition

409 In the MdL-stimulation experiments above, pharmacological blockade of inhibition
410 increased APs in MOC neurons. We next asked how the effect of inhibition on MOC activity
411 would change when excitatory and inhibitory pathways were stimulated with the in vivo-like
412 synaptic timing that we observed in the AN-stimulation experiments. However, the short window
413 of time for wedge-slice viability for AN-stimulation experiments made the additional
414 pharmacological experiments necessary for testing the effect of inhibition on MOC neuron activity
415 prohibitive. Therefore, we built a computational model of an MOC neuron to test the integration
416 of excitation and inhibition with synaptic inputs that mimic AN-stimulation experiments. The
417 model MOC neuron had topology generated from a published MOC neuron morphology (Figure
418 9[47], **Figure 7A**), and ion channels and biophysical properties were tuned to mimic the recorded
419 synaptic and AP activity of MOC neurons (Methods).

420 The model MOC neuron responded to synaptic inputs based on recorded mini-EPSPs
421 (mEPSP) and mini-IPSPs (mIPSP) with closely matched amplitudes and waveforms (**Figure 7B,**
422 **Bi**), confirming that the model MOC neuron responds to synaptic inputs similarly to biological
423 MOC neurons. Next, synaptic potentials were simulated within the model MOC neuron to mimic
424 PSPs evoked from MdL-stimulation experiments both in control conditions, and with
425 pharmacological blockade of inhibitory synaptic inputs (**Figure 7C, Ci**). IPSPs were then added
426 to the model to mimic MdL-stimulation conditions, with the IPSP onset being longer latency than
427 the EPSP onset by +2.8 ms (E-I latency difference +2.8 ms), as measured in MOC neuron MdL-
428 stimulation recordings (**Figure 7C, D**).

429 The responses of the model MOC neuron to repeated synaptic inputs were then tested by
430 comparing model responses to activity recorded in MOC neurons in response to 100 Hz trains of
431 MdL-stimulation (**Figure 6, Figure 7E**). Trains of MdL-PSPs were simulated within the model,
432 first using the relative timing of excitatory and inhibitory synaptic inputs recorded during MdL-
433 stimulation as above (E-I latency difference: +2.8 ms) and then with IPSPs absent to mimic

pharmacological blockade of IPSPs in MOC neuron recordings (**Figure 7F**). Consistent with patch-clamp data, single control PSPs (EPSPs + IPSPs) did not evoke APs in the model MOC neuron. However, summation of PSPs evoked APs (latency 38.5 ms), similar to the latency to AP in MdL-stimulation experiments (49.75±29.06 ms). IPSPs were then removed from the model and summation of EPSPs initiated APs with a shorter latency (24.4 ms). This decrease in latency to APs in the absence of IPSPs is consistent with recordings from MOC neurons, and consistent with inhibition delaying APs.

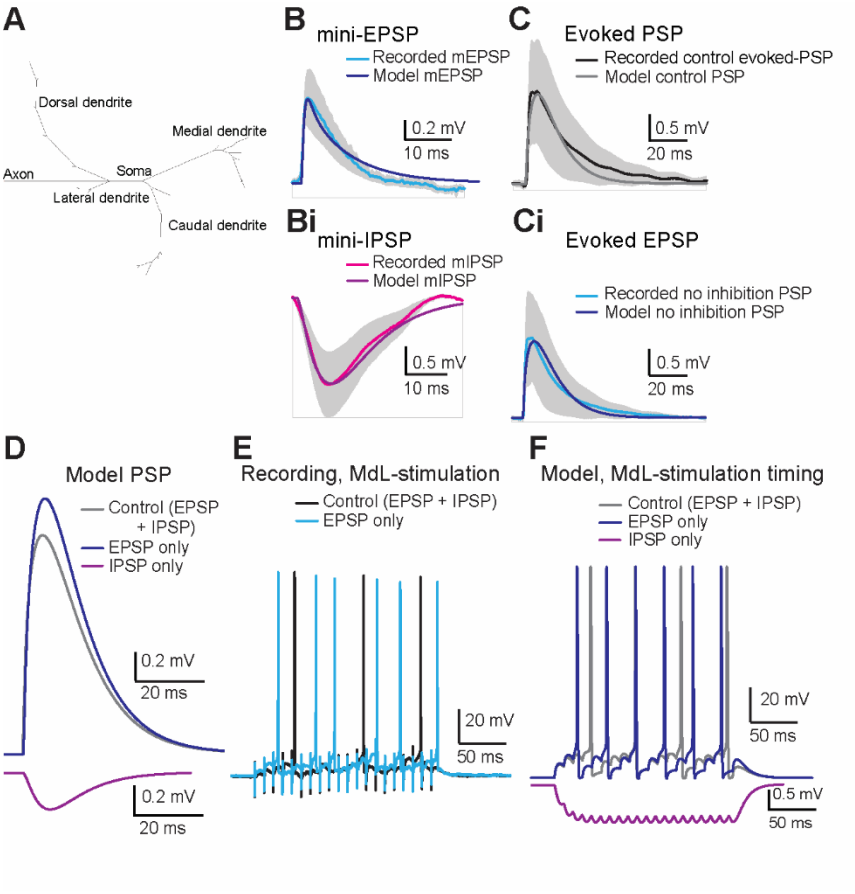

Figure 7. A computational MOC model replicates responses to MdL-stimulation. A. Topology of the model MOC neuron. B. Waveform of mEPSPs from MOC neuron recordings (light blue line, grey shading indicates standard deviation) with overlaid mEPSP generated from the model MOC neuron (dark blue). Bi. Waveform of mIPSPs from MOC neuron recordings (magenta line, grey shading indicates standard deviation) with an overlaid mIPSP generated from the model MOC neuron (purple). C. Waveform of control evoked PSPs from MOC neuron recordings (combined EPSP and IPSP, black line, grey shading indicates standard deviation) overlaid with PSPs from the model MOC neuron in control conditions (combined EPSP and IPSP,

grey line). Ci. Waveform of excitatory evoked-PSP from MOC neuron recordings after pharmacological block of inhibitory receptors (no inhibition, EPSP only, blue line, grey shading indicates standard deviation) overlaid with PSPs from the model MOC neuron with excitatory PSPs only (no inhibition, EPSP only, dark blue line). D. Comparison of model evoked-PSPs in control (EPSP and IPSP, grey), excitatory only (inhibition removed, EPSP only, dark blue), and inhibitory only conditions (excitation removed, IPSP only, purple). E. Current-clamp recordings from MOC neurons during 100 Hz, 20 pulse MdL-stimulation to evoke APs in control (evoked EPSP and IPSP, black), and excitatory only conditions (inhibition blocked, EPSP only, blue). F. Response of the model MOC neuron to PSPs simulated at 100 Hz, 20 pulse trains with synaptic timing mimicking MdL-stimulation synaptic timing in control (EPSP and IPSP, grey), excitatory only (inhibition removed, EPSPs only, dark blue), and inhibitory only conditions (excitation removed, IPSP only, purple).

We next used the MOC neuron model to determine how the timing of inhibition relative to excitation affects MOC neuron activity in the in vivo-like AN-stimulation configuration. In this configuration, the median latency to synaptic inhibition is closer to that of synaptic excitation compared to the greater synaptic timing separation in the MdL-stimulation configuration, and in some cells, inhibition preceded excitation (see Figure 3,4). We first generated single PSPs with varying excitatory and inhibitory synaptic timing ranging from EPSPs preceding IPSPs from 0 to 10 ms in 1 ms increments (E-I latency difference 0 to +10 ms), and IPSPs preceding EPSPs from 0 to 10 ms in 1 ms increments (E-I latency difference 0 to -10 ms). Integrated PSPs generated from these combinations had systematically varying amplitudes (**Figure 8A**). Simulating PSPs with the most extreme observed E-I latencies from AN-stimulation recordings also resulting in integrated PSPs with varying amplitudes (**Figure 8B**).

We then simulated trains of PSPs in the MOC model to analyze the effect of synaptic timing on AP latency and rate. PSPs with E-I latencies from -10 to +10 ms were simulated at rates of 100 Hz. PSPs summated to evoke APs with latencies and rates that systematically varied depending on E-I latency difference (**Figure 8C**). With only EPSPs (IPSPs removed), model APs occurred at 31.5 Hz. Adding simulated inhibitory PSPs during train stimulation increased the latency to the first AP and reduced AP rate in all cases. The degree of the effect of inhibition depended on the E-I latency difference, with the most effective inhibition occurring with E-I latency differences of -10, -1, and +9 ms (AP latency: ~48 ms, AP rate: ~20 Hz), and the least effective inhibition occurring with E-I latency differences of -6.0 and +4.0 ms (AP latency: ~43 ms, AP rate: ~23.5 Hz). In wedge-slice recordings with AN-stimulation, E-I latency differences in all cells ranged from -4.4 ms to +3.5 ms, a range that nearly includes both minimal and maximal effects of

inhibition on increasing AP latency and decreasing AP rate. Notably, the median AN-evoked E-I latency difference (+0.4 ms) had a greater effect on delaying and decreasing the rate of APs compared to the median MdL-evoked E-I latency difference (+2.8 ms) (**Figure 8D**), indicating that inhibitory synaptic inputs have a greater effect on suppressing APs in MOC neurons when occurring with the in vivo-like timing measured in AN-stimulation experiments. However, there was a much reduced effect of inhibition if the IPSP amplitude was decreased to match recordings in which background MNTB activity caused synaptic depression of IPSPs[19] (**Figure 8D**). The variability in timing of inhibitory inputs recorded in different MOC neurons paired with the degree of prior synaptic depression suggests that inhibition may have a different effect on each MOC neuron in the brain, and can thus flexibly adjust MOC neuron activity and de-synchronize the population of MOC neurons.

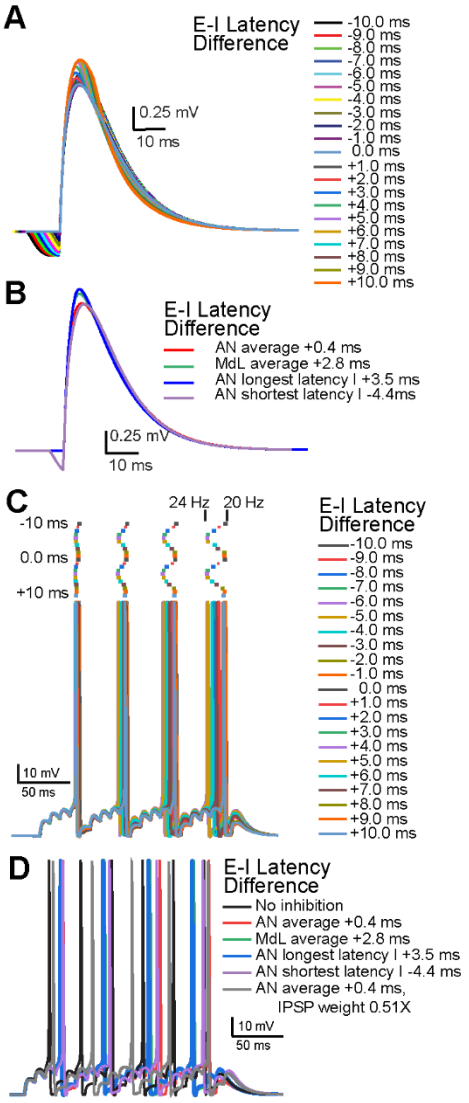

Figure 8. Varying latencies of summating EPSPs and IPSPs adjust model MOC neuron AP onset and rate. A. PSPs in the model MOC neuron resulting from summation of EPSPs and IPSPs at the E-I latency differences indicated. B. PSPs in the model MOC neuron resulting from summation of EPSPs and IPSPs at E-I latency differences from recorded MOC neurons. C. APs in the model MOC neuron resulting from summation of 100 Hz trains of simulated EPSPs and IPSPs at the E-I latency differences indicated. Raster plots above the APs indicate timing of AP peak. Changing E-I Latency Differences adjusted the AP rate between ~20 and 24 Hz, indicated above the rasters. D. APs in the model MOC neuron resulting from summation of simulated EPSPs and IPSPs with E-I latency differences recorded in MOC neurons, or with reduced a IPSP amplitude (0.51 times the control value) to mimic prior synaptic depression.

Together, our results indicate that inhibition from the MNTB can delay initial spiking of MOC neurons, and that the precise timing of inhibition can flexibly adjust MOC activity rates. In addition, the inhibitory pathway to MOC neurons is exceptionally fast and precise, due to the properties of synaptic transmission and neuron function localized to the AN synapses onto CN cells, the CN cells themselves, and CN projection axons.

Discussion

MOC neuron activity

Diverse synaptic inputs to MOC neurons likely converge to adjust MOC function under changing hearing conditions. The sound responses of MOC neurons in vivo have low thresholds, V-shaped tuning curves, sound-evoked firing rates up to 110 Hz, and a variable latency from sound onset to APs that decreases with loud sounds[24,25,48–50]. Histological and lesion experiments have shown synaptic inputs to MOC neurons from a variety of auditory and non-auditory neurons[36,38,39,51–62]. In vitro patch-clamp recordings of synaptic inputs to MOC neurons include functional demonstration of ascending excitatory synaptic inputs from CN T-stellate cells[17] and possibly CN SCC neurons[37], as well as descending, facilitating excitatory synaptic inputs from the IC[17]. Inhibitory synaptic inputs were recorded in putative MOC neurons[63] and more recently originating in the MNTB as shown in genetically identified MOC neurons[18]. Serotonergic excitation of MOC neurons[64] suggests function of additional modulatory inputs. These diverse inputs likely underestimate the convergence of synaptic inputs to MOC neurons. The in vitro wedge-slice preparation combined with machine learning and single-neuron computational modeling used here is a first step in probing synaptic integration in MOC neurons in vitro, from monaural ascending circuits with in vivo-like timing.

Functional synaptic inputs to MOC neurons

The wedge-slice includes the monaural ascending circuitry to MOC neurons beginning with AN axon terminals from Type I SGN onto CN neurons including GBC, T-stellate cells, and other CN cells. CN axons projecting to the SOC are intact[32]. Type II SGN terminations in the CN including onto granule and other cells[65–67] are also present. Intrinsic CN circuitry remains intact, including excitatory and inhibitory connections within the CN[68–80] and reciprocal connectivity between bushy[81] and T-stellate cells[82]. Absent from the preparation are the cochlea, commissural

544 pathways between the CN, and most descending circuits to the CN. While we did not determine
545 the cell types generating synaptic responses in MOC neurons, the varied patterns of multiple peaks
546 of PSCs, found both in AN- and MdL-stimulation experiments, suggest diverse excitatory and
547 inhibitory inputs. These patterns suggest either additional direct CN projections, or poly-synaptic
548 inputs with a contralateral CN origin. Additional potential sources of excitation are SCC neurons[37],
549 axon collaterals from the GBCs[83,84], or other as-yet unidentified sources. For inhibition, there may
550 be an additional direct projection from the CN[85], but poly-synaptic inputs are likely because of the
551 ~3-4 ms delay between first and second clusters of IPSCs in most recordings. Potential poly-
552 synaptic inhibitory inputs from auditory neurons include the LNTB[86,87], the superior peri-olivary
553 nucleus (SPON)[88,89], other inhibitory neurons in the VNTB[90], or the MOC neurons themselves,
554 which are cholinergic but likely also GABAergic[91–93].
555
556 *Speed and fidelity of the GBC–MNTB inhibitory pathway*
557 The GBC-MNTB pathway inhibits many other SOC neurons, including the LSO, MSO,
558 lateral olivocochlear neurons (LOC), and SPON neurons. The pathway has large Endbulb of Held
559 synapses from the AN onto the GBCs, while the GBCs have large diameter, heavily myelinated
560 axons[29,94–96], and a termination in the large Calyx of Held onto MNTB neurons. High fidelity
561 synaptic transfer throughout the pathway allows activity up to hundreds of Hz[94,97–100,101–113]. The
562 high speed of this pathway was demonstrated in the GBC–MNTB synapses to the MSO[28] in
563 gerbils. In our present results in mice, in two MOC neuron recordings the inhibitory pathway is
564 shorter latency than the excitatory pathway, despite having an additional synapse, indicating that
565 despite lacking some of the axonal GBC specializations that are present in gerbils[31], mice also
566 have an exceptionally fast GBC-MNTB pathway. However, in our results the excitatory pathway
567 on average has a shorter latency than the inhibitory pathway. One interpretation of this is that in
568 addition to the inhibitory pathway being fast, the excitatory pathway is also exceptionally fast,
569 which is unexpected due to the ~5 ms AP latency in T-stellate cells[114]. Another possibility is that
570 MNTB axon branches to MOC neurons are slower conducting compared to MNTB axon branches
571 to MSO neurons.
572 Our results also pinpoint the segments of the inhibitory pathway responsible for both its
573 speed and precision by directly comparing the relative latency differences, jitter, and response
574 probability between EPSCs and IPSCs evoked using MdL- vs AN-stimulation. Studies have

575 indicated that, although GBC's have large[33,34,43,115], often supra-threshold[45,70,115,116] PSPs, some
576 amount of synaptic summation is required for the precise phase-locking and enhanced entrainment
577 of GBC's[33–35,114] that is also attributed to a low somatic resistance with a short temporal integration
578 window[43,45,117]. In our results, addition of the CN with AN-stimulation reduces the probability of
579 activity in the pathway, confirming that there is not a 1:1 PSP:AP relationship and that synaptic
580 summation contributes to the 'coincidence detector' function of GBC's. There may also be
581 species-specific circuit differences, intact inhibitory CN circuits, decreased release probability
582 from AN axons, or smaller post-synaptic responses in the GBC. Our observed decreased latency
583 of inhibitory PSCs relative to excitatory PSCs was also only apparent when the circuit included
584 the full CN via AN-stimulation, not with MdL-stimulation that lacked GBC participation,
585 pinpointing the speed of the inhibitory pathway to the CN and GBCs. Finally, with MdL-
586 stimulation, the inhibitory pathway has more synaptic jitter than the excitatory pathway. However,
587 this is compensated for in the AN-stimulation experiments to result in equal total jitter between
588 the excitatory and inhibitory pathways. In accordance with the precision of the endbulb of Held–
589 GBC synapse[72], this suggests that this portion of the inhibitory pathway that is added during AN-
590 stimulation experiments relative to MdL-stimulation experiments is so precise that it can
591 compensate for increased jitter at later synapses.
592
593 *Integration of excitation and inhibition at MOC neurons*
594 Our findings from both AN-stimulation experiments in wedge-slices and the computational
595 MOC model inform knowledge of the role of integration of synaptic inhibition and excitation on
596 MOC neurons both at the single cell and the population level. The presence of any inhibition in
597 the model reduced AP rates from control values. In recordings, inhibition was variable and
598 sometimes shorter latency relative to excitation. Then, in the MOC neuron computational model,
599 changing synaptic timing to reflect the different latencies of EPSCs relative to IPSCs (E-I latency
600 difference) resulted in variable amplitude summed PSPs and variable AP rates. E-I latency
601 differences that corresponded to values from MOC neuron recordings ranged from having a
602 minimal effect on reducing AP rates when inhibition lags excitation, to having the maximal effect
603 when inhibition slightly precedes excitation by ~1 ms. Interestingly, the most striking example in
604 which inhibition preceded excitation by 4.4 ms did not have the strongest effect on MOC AP rates
605 in the model, suggesting that closely-timed synaptic inhibition and excitation are most effective at

606 reducing MOC neuron activity. Further, we speculate that if the timing of inhibition is different
607 across the population of MOC neurons, in addition to the more variable excitatory timing, each
608 cell will have slightly different AP latencies and rates in response to a sound, thus de-synchronizing
609 MOC activity across the population.

610 Our results present a model that while MOC neurons receive rapid and precise excitation
611 at the single cell level, multiple mechanisms are in place to syncopate, broaden, and smooth
612 activity at the population level. This extends from broadly tuned inhibitory inputs[18], variable
613 axonal projection patterns in the cochlea [24,25,118–122], low synaptic release probability paired with
614 synaptic facilitation at MOC axon terminals onto cochlear outer hair cells (OHC)[123], and a slow
615 post-synaptic response in the OHC. Our results add fast and precisely timed synaptic inhibition to
616 the list of mechanisms to smooth MOC efferent activity, which paradoxically adds imprecision to
617 the MOC system to exert slow effects on cochlear gain control.
618

619 **Methods Summary**

620 Asymmetric 'wedge slice' brain slices were used to perform patch-clamp recordings from
621 identified MOC neurons in ChAT-IRES-Cre; tdTomato P13-21 mice. Electrical stimulation of pre-
622 synaptic axons either at the midline (MdL) or at the intact auditory nerve (AN) root projecting into
623 the contralateral cochlear nucleus (CN) evoked multicomponent post-synaptic currents (PSCs)
624 consisting of both excitatory and inhibitory inputs. During current-clamp recordings, post-synaptic
625 potentials (PSP) were evoked by MdL stimulation of pre-synaptic axons in the presence and
626 absence of blockers of inhibitory neurotransmission (50 μM gabazine, 1 μM strychnine), to test
627 the effect of inhibition on PSP summation. Calcium imaging in wedge slices of Atoh7/Math5 Cre;
628 GCaMP6f during AN stimulation was performed with and without blockers of glutamatergic
629 receptors (5 μM CNQX, 50 μM APV) to ensure that AN stimulation acted via synaptic, not direct
630 electrical, excitation of CN neurons. A machine learning RandomForest paradigm was trained to
631 classify EPSCs and IPSCs recorded in MdL stimulation experiments for which excitatory vs
632 inhibitory PSC identity was known, then the trained machine learning paradigm was used to
633 classify PSCs from AN experiments for which excitatory vs inhibitory identity was unknown. A
634 computational model of a single MOC neuron was designed based on properties recorded from
635 MOC neurons, then synaptic inputs were simulated within the model to reflect the varying
636 latencies of excitatory and inhibitory synaptic inputs recorded in MOC neurons with MdL vs AN
637 stimulation.

638

639

640 **Acknowledgements:**

641 Thank you to Dr. Lena Ebbers and Dr. Hans Nothwang from Carl von Ossietzky Universität
642 Oldenburg for the Atoh7/Math5 Cre mice. Thank you to Dr. Kirupa Suthakar for thoughtful
643 discussions and a critical reading of the manuscript. This research was supported by the
644 Intramural Research Program of the NIH, NIDCD, Z01 DC000091 (CJCW) and the
645 Bioinformatics and Biostatistics Core of the NIH / NIDCD.

646

647 **References**

648 1. Ashmore, J. *et al.* The remarkable cochlear amplifier. *Hear. Res.* **266**, 1–17 (2010).

649 2. Fettiplace, R. & Hackney, C. M. The origin of the cochlear amplifier. *Hear. Res.* (2010)
650 doi:10.1016/j.heares.2009.12.011.

651 3. Dallos, P. The active cochlea. *J. Neurosci.* **12**, 4575–4585 (1992).

652 4. Oghalai, J. S. The cochlear amplifier: augmentation of the traveling wave within the inner
653 ear. *Curr. Opin. Otolaryngol. Head Neck Surg.* **12**, 431–8 (2004).

654 5. Fex, J. Efferent inhibition in the cochlea related to hair-cell dc activity: study of
655 postsynaptic activity of the crossed olivocochlear fibres in the cat. *J. Acoust. Soc. Am.* **41**,
656 666–75 (1967).

657 6. Mountain, D. C. Changes in endolymphatic potential and crossed olivocochlear bundle
658 stimulation alter cochlear mechanics. *Science (80-.).* **210**, 71–72 (1980).

659 7. Siegel, J. H. & Kim, D. O. Efferent neural control of cochlear mechanics? Olivocochlear
660 bundle stimulation affects cochlear biomechanical nonlinearity. *Hear. Res.* **6**, 171–182
661 (1982).

662 8. Guinan, J. J. Physiology of Olivocochlear Efferents. in *The Cochlea: Springer Handbook*
663 *of Auditory Research* (eds. Dallos, P., Fay, R. & Popper, A.) 435–502 (Springer-Verlag,
664 1996).

665 9. Guinan, J. J. Cochlear efferent innervation and function. *Curr. Opin. Otolaryngol. Head*
666 *Neck Surg.* **18**, 447–453 (2010).

667 10. Elgoyhen, A. B. & Katz, E. The efferent medial olivocochlear-hair cell synapse. *J.*
668 *Physiol. Paris* **106**, 47–56 (2012).

669 11. Kawase, T., Delgutte, B. & Liberman, M. C. Antimasking effects of the olivocochlear
670 reflex. II. Enhancement of auditory-nerve response to masked tones. *J. Neurophysiol.* **70**,
671 2533–2549 (1993).

672 12. Guinan, J. J. *Physiology of the Medial and Lateral Olivocochlear Systems*. (2011).
673 doi:10.1007/978-1-4419-7070-1.

674 13. Winslow, R. L. & Sachs, M. B. Effect of electrical stimulation of the crossed
675 olivocochlear bundle on auditory nerve response to tones in noise. *J. Neurophysiol.* **57**,
676 1002–1021 (1987).

677 14. Rajan, R. Involvement of Cochlear Efferent Pathways in Protective Effects Elicited with

678 Binaural Loud Sound Exposure in Cats. *J. Neurophysiol.* **74**, 582–597 (1995).
679 15. Reiter, E. R. & Liberman, M. C. Efferent-mediated protection from acoustic
680 overexposure: relation to slow effects of olivocochlear stimulation. *J. Neurophysiol.* **73**,
681 506–514 (1995).
682 16. Terreros, G., Jorratt, P., Aedo, C., Elgoyhen, A. B. & Delano, P. H. Selective Attention to
683 Visual Stimuli Using Auditory Distractors Is Altered in Alpha-9 Nicotinic Receptor
684 Subunit Knock-Out Mice. **36**, 7198–7209 (2016).
685 17. Romero, G. E. & Trussell, L. O. Distinct forms of synaptic plasticity during ascending vs
686 descending control of medial olivocochlear efferent neurons. *Elife* **10**, (2021).
687 18. Torres Cadenas, L., Fischl, M. J. & Weisz, C. J. C. Synaptic Inhibition of Medial
688 Olivocochlear Efferent Neurons by Neurons of the Medial Nucleus of the Trapezoid
689 Body. *J. Neurosci.* **40**, 509–525 (2020).
690 19. Torres Cadenas, L., Cheng, H. & Weisz, C. J. C. Synaptic plasticity of inhibitory synapses
691 onto medial olivocochlear efferent neurons. *J. Physiol.* **600**, 2747–2763 (2022).
692 20. Tong, H. *et al.* Protection from noise-induced hearing loss by kv2.2 potassium currents in
693 the central medial olivocochlear system. *J. Neurosci.* **33**, 9113–21 (2013).
694 21. Sinclair, J. L., Barnes-Davies, M., Kopp-Scheinpflug, C. & Forsythe, I. D. Strain-specific
695 differences in the development of neuronal excitability in the mouse ventral nucleus of the
696 trapezoid body. *Hear. Res.* **354**, 28–37 (2017).
697 22. Fex, J. Single fibre analysis of crossed efferent fibres. *Acta Physiol. Scand.* **55**, 7–32
698 (1962).
699 23. Robertson, D. & Gummer, M. Physiological and morphological characterization of
700 efferent neurones in the guinea pig cochlea. *Hear. Res.* **20**, 63–77 (1985).
701 24. Liberman, M. C. & Brown, M. C. Physiology and anatomy of single olivocochlear
702 neurons in the cat. *Hear. Res.* **24**, 17–36 (1986).
703 25. Brown, M. C. Morphology and response properties of single olivocochlear fibers in the
704 guinea pig. *Hear. Res.* **40**, 93–109 (1989).
705 26. Robertson, D. Horseradish peroxidase injection of physiologically characterized afferent
706 and efferent neurones in the guinea pig spiral ganglion. *Hear. Res.* **15**, 113–21 (1984).
707 27. Jercog, P. E., Svirskis, G., Kotak, V. C., Sanes, D. H. & Rinzel, J. Asymmetric excitatory
708 synaptic dynamics underlie interaural time difference processing in the auditory system.

709 *PLoS Biol.* **8**, e1000406 (2010).
710 28. Roberts, M. T., Seeman, S. C. & Golding, N. L. A mechanistic understanding of the role
711 of feedforward inhibition in the mammalian sound localization circuitry. *Neuron* **78**, 923–
712 35 (2013).
713 29. Ford, M. C. *et al.* Tuning of Ranvier node and internode properties in myelinated axons to
714 adjust action potential timing. *Nat. Commun.* **6**, 1–14 (2015).
715 30. Brand, A., Behrend, O., Marquardt, T., McAlpine, D. & Grothe, B. Precise inhibition is
716 essential for microsecond interaural time difference coding. *Nature* **417**, 543–547 (2002).
717 31. Stange-Marten, A. *et al.* Input timing for spatial processing is precisely tuned via constant
718 synaptic delays and myelination patterns in the auditory brainstem. *Proc. Natl. Acad. Sci.*
719 **114**, E4851–E4858 (2017).
720 32. Fischl, M. J. & Weisz, C. J. C. In Vitro Wedge Slice Preparation for Mimicking In Vivo
721 Neuronal Circuit Connectivity. *J. Vis. Exp.* (2020) doi:10.3791/61664.
722 33. Rhode, W. S., Oertel, D., Smith, P. H., Oertel, D. & Smith, P. H. Physiological response
723 properties of cells labeled intracellularly with horseradish peroxidase in cat ventral
724 cochlear nucleus. *J. Comp. Neurol.* **213**, 448–463 (1983).
725 34. Smith, P. H. & Rhode, W. S. Characterization of HRP-labeled globular bushy cells in the
726 cat anteroventral cochlear nucleus. *J. Comp. Neurol.* **266**, 360–375 (1987).
727 35. Joris, P. X., Carney, L. H., Smith, P. H. & Yin, T. C. Enhancement of neural
728 synchronization in the anteroventral cochlear nucleus. I. Responses to tones at the
729 characteristic frequency. *J. Neurophysiol.* **71**, 1022–36 (1994).
730 36. Brown, M. C., Mukerji, S., Drottar, M., Windsor, A. M. & Lee, D. J. Identification of
731 inputs to olivocochlear neurons using transneuronal labeling with pseudorabies virus
732 (PRV). *J. Assoc. Res. Otolaryngol.* **14**, 703–17 (2013).
733 37. Hockley, A., Wu, C. & Shore, S. E. Olivocochlear projections contribute to superior
734 intensity coding in cochlear nucleus small cells. *J. Physiol.* (2021) doi:10.1113/JP282262.
735 38. De Venecia, R. K., Liberman, M. C., Guinan, J. J. & Brown, M. C. Medial olivocochlear
736 reflex interneurons are located in the posteroventral cochlear nucleus: A kainic acid lesion
737 study in guinea pigs. *J. Comp. Neurol.* **487**, 345–360 (2005).
738 39. Darrow, K., Benson, T. E. & Brown, M. C. Planar multipolar cells in the cochlear nucleus
739 project to medial olivocochlear neurons in mouse. *J. Comp. Neurol.* **520**, 1365–75 (2012).

740 40. Kronander, E., Michalski, N., Lebrand, C., Hornung, J.-P. & Schneggenburger, R. An
741 organotypic slice culture to study the formation of calyx of Held synapses in-vitro. *PLoS*
742 *One* **12**, e0175964 (2017).
743 41. Yang, Z., Ding, K., Pan, L., Deng, M. & Gan, L. Math5 determines the competence state
744 of retinal ganglion cell progenitors. *Dev. Biol.* **264**, 240–254 (2003).
745 42. Chen, T.-W. *et al.* Ultrasensitive fluorescent proteins for imaging neuronal activity.
746 *Nature* **499**, 295–300 (2013).
747 43. Cao, X.-J. & Oertel, D. Auditory Nerve Fibers Excite Targets Through Synapses That
748 Vary in Convergence, Strength, and Short-Term Plasticity. *J. Neurophysiol.* **104**, 2308–
749 2320 (2010).
750 44. Yang, Y., Ramamurthy, B., Neef, X. A. & Xu-friedman, M. A. Low Somatic Sodium
751 Conductance Enhances Action Potential Precision in Time-Coding Auditory Neurons. **36**,
752 11999–12009 (2016).
753 45. Oertel, D. Synaptic responses and electrical properties of cells in brain slices of the mouse
754 anteroventral cochlear nucleus. *J. Neurosci.* **3**, 2043–2053 (1983).
755 46. Cao, X. J., Shatadal, S. & Oertel, D. Voltage-sensitive conductances of bushy cells of the
756 mammalian ventral cochlear nucleus. *J. Neurophysiol.* **97**, 3961–3975 (2007).
757 47. Brown, M. C. & Levine, J. L. Dendrites of medial olivocochlear neurons in mouse.
758 *Neuroscience* **154**, 147–59 (2008).
759 48. Robertson, D. & Gummer, M. Physiological and morphological characterization of
760 efferent neurones in the guinea pig cochlea. *Hear. Res.* **20**, 63–77 (1985).
761 49. Fex, J. Single Fibre Analysis of Crossed Efferent Fibres. *Acta Physiol. Scand.* **55**, 7–32
762 (1962).
763 50. Liberman, M. C. Physiology of cochlear efferent and afferent neurons: Direct comparisons
764 in the same animal. *Hear. Res.* **34**, 179–191 (1988).
765 51. Horvath, M. *et al.* Intracochlear injection of pseudorabies virus labels descending auditory
766 and monoaminerg projections to olivocochlear cells in guinea pig. *Eur. J. Neurosci.* **18**,
767 1439–1447 (2003).
768 52. Ota, Y., Oliver, D. L. & Dolan, D. F. Frequency-Specific Effects on Cochlear Responses
769 During Activation of the Inferior Colliculus in the Guinea Pig. *J. Neurophysiol.* **91**, 2185–
770 2193 (2004).

771 53. Gómez-Nieto, R., Rubio, M. E. & López, D. E. Cholinergic input from the ventral nucleus
772 of the trapezoid body to cochlear root neurons in rats. *J. Comp. Neurol.* **506**, 452–68
773 (2008).
774 54. Suthakar, K. & Ryugo, D. K. Descending Projections from the Inferior Colliculus to
775 Medial Olivocochlear Efferents: Mice with Normal Hearing, Early Onset Hearing Loss,
776 and Congenital Deafness. *Hear. Res.* (2016) doi:10.1016/j.heares.2016.06.014.
777 55. Benson, T. E. & Brown, M. C. Ultrastructure of synaptic input to medial olivocochlear
778 neurons. *J Comp Neurol* **499**, 244–57 (2006).
779 56. Faye-Lund, H. Projection from the inferior colliculus to the superior olivary complex in
780 the albino rat. *Anat. Embryol. (Berl).* **175**, 35–52 (1986).
781 57. Caicedo, A. & Herbert, H. Topography of descending projections from the inferior
782 colliculus to auditory brainstem nuclei in the rat. *J. Comp. Neurol.* **328**, 377–92 (1993).
783 58. Thompson, A. M. & Thompson, G. C. Relationship of descending inferior colliculus
784 projections to olivocochlear neurons. *J. Comp. Neurol.* **335**, 402–412 (1993).
785 59. Vetter, D. E., Saldaña, E. & Mugnaini, E. Input from the inferior colliculus to medial
786 olivocochlear neurons in the rat: a double label study with PHA-L and cholera toxin.
787 *Hear. Res.* **70**, 173–86 (1993).
788 60. Mulders, W. H. A. M. & Robertson, D. Inputs from the cochlea and the inferior colliculus
789 converge on olivocochlear neurones. *Hear. Res.* **167**, 206–213 (2002).
790 61. Mulders, W. H. A. M. & Robertson, D. Evidence for direct cortical innervation of medial
791 olivocochlear neurones in rats. *Hear. Res.* **144**, 65–72 (2000).
792 62. Groff, J. A. & Liberman, M. C. Modulation of cochlear afferent response by the lateral
793 olivocochlear system: activation via electrical stimulation of the inferior colliculus. *J.*
794 *Neurophysiol.* **90**, 3178–200 (2003).
795 63. Robertson, D. Physiology and Morphology of Cells in the Ventral Nucleus of Trapezoid
796 Body and Rostral Periolivary Regions of the Rat Superior Olivary Complex Studied in
797 Slices. *Audit. Neurosci.* **2**, 15–31 (1996).
798 64. Suthakar, K. & Weisz, C. J. C. Serotonergic Modulation of Medial Olivocochlear
799 Neurons. (2023).
800 65. Berglund, A. M., Benson, T. E. & Brown, M. C. Synapses from labeled type II axons in
801 the mouse cochlear nucleus. *Hear. Res.* **94**, 31–46 (1996).

802 66. Benson, T. E. & Brown, M. C. Postsynaptic targets of type II auditory nerve fibers in the
803 cochlear nucleus. *J. Assoc. Res. Otolaryngol.* **5**, 111–25 (2004).
804 67. Weisz, C. J. C. *et al.* Outer hair cell glutamate signaling through type II spiral ganglion
805 afferents activates neurons in the cochlear nucleus in response to non-damaging sounds. *J.*
806 *Neurosci.* (2021) doi:10.1523/JNEUROSCI.0619-20.2021.
807 68. Arnott, R. H., Wallace, M. N., Shackleton, T. M. & Palmer, A. R. Onset neurones in the
808 anteroventral cochlear nucleus project to the dorsal cochlear nucleus. *JARO - J. Assoc.*
809 *Res. Otolaryngol.* **5**, 153–170 (2004).
810 69. Xie, R. & Manis, P. B. Glycinergic synaptic transmission in the cochlear nucleus of mice
811 with normal hearing and age-related hearing loss. *J. Neurophysiol.* **110**, 1848–59 (2013).
812 70. Rhode, W. S. & Greenberg, S. Lateral suppression and inhibition in the cochlear nucleus
813 of the cat. *J. Neurophysiol.* **71**, 493–514 (1994).
814 71. Wickesberg, R. E. & Oertel, D. Tonotopic projection from the dorsal to the anteroventral
815 cochlear nucleus of mice. *J. Comp. Neurol.* **268**, 389–99 (1988).
816 72. Kuenzel, T. Modulatory influences on time-coding neurons in the ventral cochlear
817 nucleus. *Hear. Res.* **384**, 107824 (2019).
818 73. Xie, R. & Manis, P. B. GABAergic and glycinergic inhibitory synaptic transmission in the
819 ventral cochlear nucleus studied in VGAT channelrhodopsin-2 mice. *Front. Neural*
820 *Circuits* **8**, 1–15 (2014).
821 74. Ngodup, T., Romero, G. E. & Trussell, L. O. Identification of an inhibitory neuron
822 subtype, the l-stellate cell of the cochlear nucleus. *Elife* **9**, 1–40 (2020).
823 75. Campagnola, L. & Manis, P. B. A Map of Functional Synaptic Connectivity in the Mouse
824 Anteroventral Cochlear Nucleus. *J. Neurosci.* **34**, 2214–30 (2014).
825 76. Cant, N. B. & Benson, C. G. Parallel auditory pathways: projection patterns of the
826 different neuronal populations in the dorsal and ventral cochlear nuclei. *Brain Res Bull* **60**,
827 457–474 (2003).
828 77. Doucet, J. R. & Ryugo, D. K. Projections from the ventral cochlear nucleus to the dorsal
829 cochlear nucleus in rats. *J. Comp. Neurol.* **385**, 245–64 (1997).
830 78. Ferragamo, M. J., Golding, N. L. & Oertel, D. Synaptic inputs to stellate cells in the
831 ventral cochlear nucleus. *J Neurophysiol* **79**, 51-63. (1998).
832 79. Muniak, M. A. & Ryugo, D. K. Tonotopic organization of vertical cells in the dorsal

833 cochlear nucleus of the CBA/J mouse. *J. Comp. Neurol.* **522**, 937–949 (2014).
834 80. Ostapoff, E. M., Morest, D. K. & Parham, K. Spatial organization of the reciprocal
835 connections between the cat dorsal and anteroventral cochlear nuclei. *Hear. Res.* **130**, 75–
836 93 (1999).
837 81. Gómez-Nieto, R. & Rubio, M. E. A bushy cell network in the rat ventral cochlear nucleus.
838 *J. Comp. Neurol.* **516**, 241–263 (2009).
839 82. Cao, X.-J., Lin, L., Sugden, A. U., Connors, B. W. & Oertel, D. Nitric Oxide-Mediated
840 Plasticity of Interconnections Between T-Stellate cells of the Ventral Cochlear Nucleus
841 Generate Positive Feedback and Constitute a Central Gain Control in the Auditory
842 System. *J. Neurosci.* **39**, 6095–6107 (2019).
843 83. Kuwabara, N., DiCaprio, R. a & Zook, J. M. Afferents to the medial nucleus of the
844 trapezoid body and their collateral projections. *J. Comp. Neurol.* **314**, 684–706 (1991).
845 84. Smith, P. H., Joris, P. X., Carney, L. H. & Yin, T. C. Projections of physiologically
846 characterized globular bushy cell axons from the cochlear nucleus of the cat. *J. Comp.*
847 *Neurol.* **304**, 387–407 (1991).
848 85. Weingarten, D. J. *et al.* An inhibitory glycinergic projection from the cochlear nucleus to
849 the lateral superior olive. 1–9 (2023) doi:10.3389/fncir.2023.1307283.
850 86. Cant, N. B. & Hyson, R. L. Projections from the lateral nucleus of the trapezoid body to
851 the medial superior olivary nucleus in the gerbil. *Hear. Res.* **58**, 26–34 (1992).
852 87. Kuwabara, N. & Zook, J. M. Projections to the medial superior olive from the medial and
853 lateral nuclei of the trapezoid body in rodents and bats. *J. Comp. Neurol.* **324**, 522–538
854 (1992).
855 88. Kulesza, R. J. & Berrebi, A. S. Superior paraolivary nucleus of the rat is a GABAergic
856 nucleus. *JARO - J. Assoc. Res. Otolaryngol.* **1**, 255–269 (2000).
857 89. Kelly, J. B., Liscum, A., Van Adel, B. & Ito, M. Projections from the superior olive and
858 lateral lemniscus to tonotopic regions of the rat's inferior colliculus. *Hear. Res.* **116**, 43–
859 54 (1998).
860 90. Albrecht, O., Dondzillo, A., Mayer, F., Thompson, J. A. & Klug, A. Inhibitory projections
861 from the ventral nucleus of the trapezoid body to the medial nucleus of the trapezoid body
862 in the mouse. *Front. Neural Circuits* **8**, 1–15 (2014).
863 91. Frank, M. M. *et al.* Experience-dependent flexibility in a molecularly diverse central-to-

peripheral auditory feedback system. *Elife* **12**, (2023).

92. Kitcher, S. R., Pederson, A. M. & Weisz, C. J. C. Diverse identities and sites of action of cochlear neurotransmitters. *Hear. Res.* (2021) doi:10.1016/j.heares.2021.108278.

93. Kitcher, S. R. & Weisz, C. J. Imaging GABAergic activity in the cochlea. (2023).

94. Brownell, W. E. Organization of the cat trapezoid body and the discharge characteristics of its fibers. *Brain Res.* **94**, 413–433 (1975).

95. Warr, W. B. Fiber degeneration following lesions in the multipolar and globular cell areas in the ventral cochlear nucleus of the cat. *Brain Res.* **40**, 247–70 (1972).

96. Lauer, A. M., Connelly, C. J., Graham, H. & Ryugo, D. K. Morphological Characterization of Bushy Cells and Their Inputs in the Laboratory Mouse (Mus musculus) Anteroventral Cochlear Nucleus. *PLoS One* **8**, 1–16 (2013).

97. Spirou, G. A., Brownell, W. E. & Zidanic, M. Recordings from cat trapezoid body and HRP labeling of globular bushy cell axons. *J. Neurophysiol.* **63**, 1169–1190 (1990).

98. Kopp-Scheinpflug, C., Tolnai, S., Malmierca, M. S. & Rübsamen, R. The medial nucleus of the trapezoid body: Comparative physiology. *Neuroscience* **154**, 160–170 (2008).

99. Guinan, J. J., Guinan, S. S. & Norris, B. E. Single auditory units in the superior olivary complex: I: Responses to sounds and classifications based on physiological properties. *Int. J. Neurosci.* **4**, 101–120 (1972).

100. Sommer, I., Lingenhöhl, K. & Friauf, E. Principal cells of the rat medial nucleus of the trapezoid body: an intracellular in vivo study of their physiology and morphology. *Exp. Brain Res.* **95**, 223–239 (1993).

101. Wu, S. H. & Kelly, J. B. Response of neurons in the lateral superior olive and medial nucleus of the trapezoid body to repetitive stimulation: intracellular and extracellular recordings from mouse brain slice. *Hear. Res.* **68**, 189–201 (1993).

102. Taschenberger, H. & von Gersdorff, H. Fine-tuning an auditory synapse for speed and fidelity: developmental changes in presynaptic waveform, EPSC kinetics, and synaptic plasticity. *J. Neurosci.* **20**, 9162–73 (2000).

103. Kopp-Scheinpflug, C., Lippe, W. R., Dörrscheidt, G. J. & Rübsamen, R. The medial nucleus of the trapezoid body in the gerbil is more than a relay: Comparison of pre- and postsynaptic activity. *JARO - J. Assoc. Res. Otolaryngol.* **4**, 1–23 (2003).

104. Kopp-Scheinpflug, C., Steinert, J. R. & Forsythe, I. D. Modulation and control of synaptic

895 transmission across the MNTB. (2011) doi:10.1016/j.heares.2011.02.007.
896 105. Kopp-Scheinpflug, C., Tolnai, S., Malmierca, M. S. & Rübsamen, R. The medial nucleus
897 of the trapezoid body: comparative physiology. *Neuroscience* **154**, 160–70 (2008).
898 106. Barnes-Davies, M. & Forsythe, I. D. Pre- and postsynaptic glutamate receptors at a giant
899 excitatory synapse in rat auditory brainstem slices. *J. Physiol.* **488 (Pt 2**, 387–406 (1995).
900 107. Mc Laughlin, M. *et al.* The interaural time difference pathway: A comparison of spectral
901 bandwidth and correlation sensitivity at three anatomical levels. *J. Assoc. Res.*
902 *Otolaryngol.* **15**, 203–218 (2014).
903 108. Guinan, J. J. & Li, R. Y. Signal processing in brainstem auditory neurons which receive
904 giant endings (calyces of Held) in the medial nucleus of the trapezoid body of the cat.
905 *Hear. Res.* **49**, 321–34 (1990).
906 109. Takahashi, T., Forsythe, I. D., Tsujimoto, T., Barnes-Davies, M. & Onodera, K.
907 Presynaptic calcium current modulation by a metabotropic glutamate receptor. *Science*
908 **274**, 594–7 (1996).
909 110. Borst, J. G., Helmchen, F. & Sakmann, B. Pre- and postsynaptic whole-cell recordings in
910 the medial nucleus of the trapezoid body of the rat. *J. Physiol.* **489 (Pt 3**, 825–40 (1995).
911 111. Smith, P. H., Joris, P. X. & Yin, T. C. Anatomy and physiology of principal cells of the
912 medial nucleus of the trapezoid body (MNTB) of the cat. *J. Neurophysiol.* **79**, 3127–3142
913 (1998).
914 112. Tolnai, S., Hernandez, O., Englitz, B., Rübsamen, R. & Malmierca, M. S. The medial
915 nucleus of the trapezoid body in rat: spectral and temporal properties vary with anatomical
916 location of the units. *Eur. J. Neurosci.* **27**, 2587–98 (2008).
917 113. Englitz, B., Tolnai, S., Typlt, M., Jost, J. & Rübsamen, R. Reliability of synaptic
918 transmission at the synapses of held in vivo under acoustic stimulation. *PLoS One* **4**,
919 (2009).
920 114. Rhode, W. S. & Smith, P. H. Encoding timing and intensity in the ventral cochlear
921 nucleus of the cat. *J. Neurophysiol.* **56**, 261–86 (1986).
922 115. Pfeiffer, R. R. Classification of response patterns of spike discharges for units in the
923 cochlear nucleus: tone-burst stimulation. *Exp. brain Res.* **1**, 220–35 (1966).
924 116. Spirou, G. A., Rager, J. & Manis, P. B. Convergence of auditory-nerve fiber projections
925 onto globular bushy cells. *Neuroscience* **136**, 843–863 (2005).

926 117. McGinley, M. J. & Oertel, D. Rate thresholds determine the precision of temporal
927 integration in principal cells of the ventral cochlear nucleus. *Hear. Res.* **216–217**, 52–63
928 (2006).
929 118. Warr, W. Organization of Olivocochlear Efferent Systems in Mammals. in *The*
930 *Mammalian Auditory Pathways: Neuroanatomy, Springer Handbook of Auditory*
931 *Research* (eds. Webster, D. B., Popper, A. & Fay, R.) 410–448 (Springer-Verlag, 1992).
932 119. Brown, M. C. Morphology of labeled efferent fibers in the guinea pig cochlea. *J Comp*
933 *Neurol* **260**, 605–618 (1987).
934 120. Vetter, D. E., Adams, J. C. & Mugnaini, E. Chemically distinct rat olivocochlear neurons.
935 *Synapse* **7**, 21–43 (1991).
936 121. Brown, M. C. Recording and Labeling at a Site along the Cochlea shows Alignment of
937 Medial Olivocochlear and Auditory-Nerve Tonotopic Mappings. *J. Neurophysiol.*
938 jn.00842.2015 (2016) doi:10.1152/jn.00842.2015.
939 122. Brown, M. C. Single-unit Labeling of Medial Olivocochlear Neurons: The Cochlear
940 Frequency Map for Efferent Axons. *J. Neurophysiol.* (2014) doi:10.1152/jn.00045.2014.
941 123. Ballestero, J. *et al.* Short-term synaptic plasticity regulates the level of olivocochlear
942 inhibition to auditory hair cells. *J. Neurosci.* **31**, 14763–74 (2011).
943 124. Carnevale, N. T. & Hines, M. L. *The Neuron Book*. (Cambridge University Press, 2006).
944 125. Paxinos, G. & Watson, K. B. *The Mouse Brain in Stereotaxic Coordinates*. (Academic
945 Press).
946
947

Supplementary Methods

RESOURCE AVAILABILITY

Materials availability

This study did not generate new unique materials.

Data and code availability

DATA

Electrophysiology and imaging data will be deposited and publicly available by the date of publication.

CODE

All original code will be deposited and will be publicly available as of the date of publication.

ANALYSIS TOOLS

Any additional information required to reanalyze the data reported in this paper is available from the lead contact upon request.

EXPERIMENTAL MODEL DETAILS

Ethical approval and animal housing

Animal procedures followed National Institutes of Health guidelines, as approved by the National Institute of Neurological Disorders and Stroke/National Institute on Deafness and Other Communication Disorders Animal Care and Use Committee. Pre-weaned mice postnatal age 13-21 (P13-P21) were used for experiments and were housed with parents and littermates before use. Mice were housed in the NIDCD animal facility with a 12:12 light/dark cycle where food and water were provided *ad libitum*. Mice of both sexes were used for experiments. For consideration of sex as a biological factor, postsynaptic currents (PSCs) recorded during stimulation of the ventral acoustic stria (‘midline stimulation’; MdL-stimulation) were analyzed and compared between the sexes (see below for complete methods). No significant differences

were found for excitatory or inhibitory PSCs using the metrics of onset latency, onset jitter, rise time, decay tau, amplitude and probability. Datasets were therefore pooled.

Median ± MAD		Onset Latency (ms)	Onset Jitter (ms)	Rise Time (ms)	Decay Tau (ms)	Amplitude (nA)	Probability
Male	EPSCs (10)	2.11 ± 0.43	0.19 ± 0.08	0.61 ± 0.28	2.44 ± 0.50	-0.05 ± 0.02	0.48 ± 0.21
Female	EPSCs (11)	2.02 ± 0.67	0.41 ± 0.15	0.73 ± 0.20	2.23 ± 0.55	-0.04 ± 0.02	0.52 ± 0.31
Male	IPSCs (8)	5.01 ± 1.98	0.53 ± 0.08	1.26 ± 0.59	5.79 ± 2.85	-0.07 ± 0.02	0.39 ± 0.11
Female	IPSCs (10)	5.30 ± 1.26	0.44 ± 0.20	1.40 ± 0.32	3.34 ± 0.48	-0.05 ± 0.02	0.25 ± 0.16

Table M1: Values for metrics analyzed for PSCs evoked with midline (MdL) stimulation for comparison of sex as a biological factor. n # for each group in parentheses represents # of peaks (clusters) analyzed. Comparisons made between sexes showed no significant differences with Mann-Whitney U Test.

ChAT-IRES-Cre x tdTomato mouse line

ChAT-IRES-Cre transgenic mice on either a C57BL/6J (RRID:IMSR_JAX:028861) or a C57BL/6N (RRID:IMSR_JAX:018957) background strain were crossed with tdTomato reporter mice (Ai14, Cre reporter allele inserted into Rosa 26 locus; RRID:IMSR_JAX:007914) to yield offspring heterozygous for each allele for experiments. These mice were used to target MOC neurons for patch-clamp recordings as previously described (Torres Cadenas et al., 2020).

Atoh7/Math5 Cre x GCaMP6f mouse line

Atoh7/Math5 Cre mice (Yang et al., 2003, RRID:MGI:3717726) were crossed with GCaMP6f Ai95(RCL-GCaMP6f, RRID:IMSR_JAX:028865) mice for use in calcium imaging experiments of cochlear nucleus bushy cells.

Brain slice preparation

Mice were killed by carbon dioxide inhalation at a rate of 20-30% of chamber volume per minute, then decapitated. The brain was removed in cold artificial cerebrospinal fluid (aCSF) containing the following (in mM): 124 NaCl, 1.2 $CaCl_2$, 1.3 $MgSO_4$, 5 KCl, 26 $NaHCO_3$, 1.25 KH_2PO_4, and 10 dextrose; 1 mM kynurenic acid was included during slice preparation. The pH was equal to 7.4 when bubbled with 95% O_2/5% CO_2. In experiments in which mini-post-synaptic potentials (mPSPs) were recorded, 1 µM tetrodotoxin (TTX) was included in the aCSF.

1006

1007 Asymmetric slices were obtained as previously described (Fischl & Weisz 2020). Briefly, the
1008 brainstem was carefully dissected from the skull to maintain a portion of the auditory nerve roots
1009 entering the cochlear nucleus, similar to methods used for thick slice preparations [27,28]. Then, a
1010 wedge-shaped section was acquired using a stage with an adjustable angle such that the lateral
1011 edge of one hemisphere was approximately 1-1.2 mm thick and contained the cochlear nucleus,
1012 and the opposite lateral edge was ~200 μm, creating a thickness of ~300-400 μm where MOC
1013 neurons were identified for patch-clamp experiments in the ventral nucleus of the trapezoid body
1014 (VNTB). An additional 300 μm slice was obtained rostral to the 'wedge slice' and used for
1015 additional experiments. For some experiments utilizing midline stimulation for evoked PSPs or
1016 for recordings of miniPSPs, symmetrical brain slices were prepared as previously described [18].
1017 Sections were transferred to an incubation chamber and maintained at 35 ± 1°C for 30-60 min.
1018 Slices then cooled to room temperature until used for experiments within 4 hours of slicing.
1019 Wedge slices were used immediately after a short recovery incubation (30 min) to improve cell
1020 viability which tends to diminish more rapidly than typical symmetrical slices due to reduced
1021 aCSF solution penetration in the larger tissue volume.

1022

1023 *Patch-clamp recordings*

1024 Sections were transferred to a recording chamber which was continuously perfused with aCSF at
1025 a rate of 5-10 mL/min. The bath temperature was held at 35 ± 1°C using an in-line heater
1026 (Warner) coupled to a temperature controller (Warner). The tissue was viewed using a Nikon
1027 Eclipse Ni-E microscope with an Apo LWD 25X/1.10 NA water-immersion objective attached
1028 to a Retiga Electro CCD camera (QImaging) operated using NIS Elements software (version
1029 4.51.01). Epifluorescence illumination with red emission filters were used to locate MOC
1030 neurons in the VNTB for recordings. Targeted cells were then observed using DIC optics for
1031 patch-clamp recordings.

1032

1033 Pipettes for patch-clamp recordings were pulled from 1.5 mm borosilicate glass capillaries to
1034 resistances between 3-7 MOhm. For voltage-clamp experiments an internal solution containing
1035 (in mM) 76 Cs-methanesulfonate, 56 CsCl, 1 $MgCl_2$, 1 $CaCl_2$, 10 HEPES, 10 EGTA, 0.3 Na-
1036 GTP, 2 Mg-ATP, 5 Na_2-phosphocreatine, 5 QX-314, and 0.01 Alexa Fluor-488 hydrazide was

1037 used. The pH was adjusted to 7.2 with CsOH. For current-clamp experiments, an internal
1038 solution containing (in mM) 125 K-gluconate, 5 KCl, 1 $MgCl_2$, 0.1 $CaCl_2$, 10 HEPES, 1 EGTA,
1039 0.3 Na-GTP, 2 Mg-ATP, 1 Na_2-phosphocreatine, and 0.01 Alexa Fluor-488 hydrazide was used.
1040 The pH was adjusted 7.2 with 1N KOH. Liquid junction potentials were -6 mV, CsCl solution
1041 and -2 mV, KGlu solution and were not adjusted for. Electrophysiology recordings were
1042 performed using a HEKA EPC10 amplifier controlled using PatchMaster NEXT (version 1.1).
1043 The recordings were sampled at 50 kHz and filtered on-line at 10 kHz. Series resistance was
1044 compensated between 60-85%. Cells were voltage-clamped at -60 mV unless stated otherwise. In
1045 current-clamp, holding currents were injected to maintain the baseline membrane potential at -60
1046 mV.
1047
1048 *Stimulation of auditory nerve and ventral acoustic stria*
1049 Post-synaptic currents (PSC) and post-synaptic potentials (PSP) recorded in MOC neurons were
1050 evoked by electrical stimulation of axons using a bipolar tungsten electrode (WPI). For auditory
1051 nerve (AN) stimulation, the electrode was lowered onto the approximate center of the auditory
1052 nerve root diameter between the cut end of the nerve and its entry into the CN. For stimulation at
1053 the midline, the electrode was placed just lateral to the midline (contralateral hemisphere to the
1054 MOC neuron recording) near the ventral surface of the tissue onto fibers of the ventral acoustic
1055 stria. The stimulation was applied with an Iso-Flex Stimulus Isolation Unit (A.M.P.I.) and the
1056 intensity was adjusted to obtain consistent amplitude postsynaptic responses in MOC neurons
1057 (stimulation range 10-2000 μA). In two experiments using AN-stimulation, the stimulus intensity
1058 was increased until the PSC latencies jumped to a shorter value (see figure 3,4), indicating direct
1059 recruitment of CN axons and bypassing of auditory nerve synapses onto CN cells. To isolate
1060 inhibitory currents in voltage-clamp, the membrane potential was clamped at 0 mV, the
1061 approximate reversal potential for AMPA-mediated glutamatergic currents. Inhibitory inputs
1062 were blocked where indicated with bath application of strychnine (1 μM) and Gabazine
1063 (SR95531, 50 μM).
1064
1065 *Miniature PSP recordings*
1066 For miniature PSP (mPSP) recordings, 1 μM tetrodotoxin (TTX, Alomone Labs) was included in
1067 the aCSF. Recordings were performed for several minutes to collect baseline (control) mPSPs.

1068 Inhibitory inputs were blocked using bath application of strychnine (1 μM) and Gabazine
1069 (SR95531, 50 μM) and gap free recordings were again taken during pharmacological
1070 manipulation. mPSPs were detected using using MiniAnalysis software version 6.0.7
1071 (Synaptosoft) using a threshold of 2 x RMS noise. PSCs were then accepted or rejected based on
1072 the characteristic PSC waveform. The decay time constants of PSCs were calculated in Mini
1073 Analysis software from individual events.
1074
1075 *Calcium Imaging*
1076 Calcium imaging of activity in CN bushy cells was performed using the Atoh7/Math5 Cre mouse
1077 line crossed with a GCaMP6f mouse line (see above). Asymmetric wedge slices were prepared
1078 as described above (Experimental Model Details). aCSF used for recording calcium signals was
1079 modified to contain 2 mM $CaCl_2$. Epifluorescence illumination with green emission filters were
1080 used to locate bushy cell neurons in the anteroventral cochlear nucleus (AVCN). The AVCN was
1081 targeted to increase the potential for imaging of globular bushy cells (GBCs) which project to the
1082 contralateral MNTB. Calcium signals were imaged using a Nikon Eclipse Ni-E microscope with
1083 an Apo LWD 25X/1.10 NA water-immersion objective in 2-photon excitation mode at 920 nm
1084 (Mai Tai HP, Spectra-Physics). A single focal plane was imaged for data collection. Imaging was
1085 performed at 3 Hz for 20 seconds using the resonant scanning galvos (Nikon Elements software
1086 version 4.51.01). Protocols consisted of 5 seconds of baseline data collection followed by
1087 auditory nerve stimulation in 3 bouts (each bout is 20 pulses at 100 Hz), at 5 seconds intervals,
1088 followed by an additional 5 seconds after the third stimulation bout, then at least 30 seconds
1089 without imaging or stimulation. Control data was acquired for several minutes before glutamate
1090 receptor blockers were applied. In a subset of experiments, CNQX (5 μM) was applied alone to
1091 block ionotropic glutamate receptors. In remaining calcium imaging experiments, APV (50 μM)
1092 was also added to additionally block NMDA receptors. Acquisition protocols were repeated
1093 during blocker application. Blockers were applied for ~10 minutes before washout. After
1094 washout, protocols were repeated to assess recovery of control conditions.
1095
1096 *Computational MOC neuron model*
1097 A model of a single MOC neuron was constructed using NEURON v8 [124] and Python 3.
1098 The neuron topology was generated from a published MOC neuron morphology (Figure 9 from,

[47]). The number of segments was empirically determined to be 86, inserted using the nseg function, and compartments were organized into larger morphological groups including the soma (length 33.6 µm, diameter 6.1 µm), axon (length 180.0 µm, diameter 1 µm), and dendrites. The three primary dendrites projected from the soma (lateral: length 12.8 µm, diameter 1 µm), dorsal (length 10.1 µm, diameter 1 µm), and medial (length 7.3 µm, diameter 1 µm). Each of these three primary dendrites branched further into 8 to 46 dendrites with lengths from 1.5 to 31.4 µm, and diameters from 1-2 µm. This detailed neuron topology allowed specific control of physiological properties. The uniform axial resistance was 210 ohm-cm, and membrane capacitance was 1 µF/cm^2. Channels were inserted into the membrane (Table 1) to recapitulate our experimental results. HCN channel reversal potential was set to -38 mV. The model was run at 35 C.

Post-synaptic potentials (PSP) were simulated at the soma to replicate recorded values. The model MOC neuron responded to synaptic inputs based on recorded mini-EPSPs (mEPSP) and mini-IPSPs (mIPSP) with output amplitudes and waveforms closely matching recorded values (mean±SD; mEPSP: amplitude: 0.86±0.23 mV, time constant of decay: 8.65±1.43 ms, n=6 neurons; mIPSP: amplitude: -1.57±1.41 mV, time constant of decay: 18.1±9.68 ms, n=7 neurons; model MOC mEPSP: amplitude: 0.90 mV, time constant of decay: 8.21 ms; model MOC mIPSP: amplitude: -1.56 mV, time constant of decay: 14.4 ms.

Next, synaptic potentials were simulated within the model MOC neuron to mimic PSPs evoked from MdL-stimulation experiments both in control conditions, and with pharmacological blockade of inhibitory synaptic inputs (MOC recording control evoked-PSP: amplitude: 1.88±0.95 mV, time constant of decay: 10.7±4.00 ms, n=9 neurons; inhibition blocked evoked-PSP (EPSP only): amplitude: 2.20±1.17 mV, time constant of decay: 14.1±7.50 ms, n=9 neurons; model MOC control evoked-PSP: amplitude: 1.64 mV, time constant of decay: 14.8 ms; model MOC inhibition blocked evoked-PSP (EPSP only): amplitude: 1.91 mV, time constant of decay: 16.4 ms. To achieve these output parameters, model MOC neuron input values were as follows: MOC model EPSP input parameters: rise time = 0.2 ms, time constant of decay = 6 ms, synaptic weight = 0.0015, reversal potential = 0 mV, resulting amplitude = 8.506 mV). The inhibitory PSP was designed so that simulation of EPSPs and IPSPs in the model replicated control MOC neuron current-clamp recordings of evoked PSPs. The model MOC IPSP output parameters were amplitude: -0.269 mV, time constant of decay: 14.8 ms. To achieve

these values, the model MOC IPSP input parameters were as follows: rise time = 2.75 ms, time constant of decay = 3.64, synaptic weight 0.00032, reversal potential = -90 mV, resulting amplitude = -0.536 mV).

PSPs with excitatory and inhibitory components were simulated with onset timing that systematically changed in 1 ms increments from excitation-inhibition latencies (E-I latency) from -10 (IPSPs precede EPSPs by 10 ms) to +10 (EPSPs precede IPSPs by 10 ms). E-I latencies were also simulated within the model to replicate recorded PSC latencies (Results text). PSPs were then simulated within the model in trains of 20 pulses at 100 Hz, using either the excitation-only PSP, or the combined PSPs with E-I latencies that systematically varied between -10 and +10, in 1 ms intervals.

The model will be available at Model dB (identifier # TBD at acceptance)

Channels	**Location (segments)**	**Conductance**
High Threshold K^+ (h.HT)	All	0.02 S/cm^2
Low Threshold K^+ (h.LT)	All	12 mS/cm^2
Low Threshold K^+ (h.kbl_LT)	All	0.6 ms^-1
H-H type Na^+ (h.na)	All	8 nS/cm^2
HCN (h.Ih_400t8)	All	12 µS/cm^2
High Threshold K^+ (h.HT)	Axon	0.32 mS/cm^2
Low Threshold K^+ (h.LT)	Axon	6 cS/cm^2
H-H type Na^+ (h.na)	Axon	9 kS/cm^2

Methods Table 1. Biophysical properties of a modeled MOC neuron compared to measured values recorded from MOC neurons.

QUANTIFICATION AND STATISTICAL ANALYSIS

Statistics for PSCs

Analysis of synaptic inputs to MOC neurons required classification of evoked PSCs as excitatory or inhibitory. Clampfit software was used to detect individual PSCs for analysis. Latency to PSC onset, rise time, latency to PSC peak, amplitude and decay time constant (tau decay) were measured for PSCs recorded at both –60 mV and 0 mV holding potential. A single exponential

function fit was used to calculate the time constant of decay (τ). These data were then used for individual cell clustering analysis (below).

Individual cell clustering analysis

Clustering analysis was performed using PSC metrics in order to sort PSCs into statistically defined clusters. Clustering was performed with PSCs collected at both –60 mV and 0 mV holding potential, when available. For each cell's PSCs, values for onset latency, rise time, amplitude and decay time constant collected from Clampfit were imported into R. Function libraries utilized for clustering included {parameters}, {factoextra} and {NbClust}. The appropriate number of clusters was determined using the gap statistic method (Tibshirani et al. 2001). This method was chosen because of its ability to select "one" as the optimal number of clusters where appropriate. The "clusGap" function was used with kmax=10 (max# of clusters), nstart=25 (# of random start centers) and B=500 (bootstrapping). Once the appropriate number of clusters was determined, a k-means cluster analysis was performed in R using the "kmeans" function to sort the PSCs into clusters (with centers=output # from gap statistic analysis and nstart=25). Once the PSCs were assigned a cluster number, statistical analyses were performed on each cluster. For PSCs collected with midline stimulation where data was acquired at 0 mV holding potential, a cluster was deemed inhibitory if it was present at both -60 mV and 0 mV. A cluster was categorized as excitatory if PSCs from the cluster were-only present at -60 mV. This was a robust categorization, with only two out of eleven cells having a PSC mis-identified in the cluster, in both cells a single excitatory PSC was classified into an inhibitory cluster (2 out of 654 mis-identified PSCs). PSCs acquired with auditory nerve (AN) stimulation were analyzed via the same cluster analysis. AN stimulation PSCs were categorized as excitatory or inhibitory using a machine learning algorithm (see below). Statistical comparisons between excitatory and inhibitory PSC clusters were then made across the population.

Machine Learning Algorithm to classify post-synaptic currents (PSCs)

A RandomForest machine learning algorithm was utilized to classify recorded PSCs as excitatory or inhibitory based on the variables of PSC rise time, time constant of decay, amplitude, probability of occurrence within a cluster, onset jitter within a cluster, peak jitter within a cluster, and animal age. All values were continuous except for animal age, which was

1185 treated as a categorical variable. The model included 952 PSCs recorded in the ML-stimulation
1186 configuration at a holding potential of -60 mV, from 22 MOC neurons. These PSCs had been
1187 previously classified as excitatory or inhibitory based on recordings from the same neurons at a
1188 holding potential of 0 mV and the clustering analysis described below. After training the
1189 RandomForest algorithm on this data, the model classification accuracy reached 99.89%, with
1190 out-of-bag (OOB) error stabilization at 150 'trees'. Re-running the algorithm on the training
1191 dataset determined that it was able to distinguish excitatory and inhibitory events perfectly with
1192 an area under the curve (AUC) of 1, indicating excellent ability of the model to distinguish
1193 excitatory vs inhibitory PSCs. The model was then used to classify the individual PSCs in the
1194 AN stimulation dataset recorded at -60 mV as excitatory or inhibitory. First, the RandomForest
1195 algorithm determined the probability that each of the 344 PSCs was excitatory or inhibitory.
1196 PSCs were given the classification that had the highest probability (>0.5) by the algorithm. The
1197 algorithm gave slightly higher classification probabilities for excitatory (0.81±0.14, n=181)
1198 compared to inhibitory (0.75±0.12, n=163) PSCs. AN stimulation PSCs were grouped into 28
1199 clusters determined above through cluster analysis. Three clusters contained both excitatory and
1200 inhibitory PSCs. Two cells had a majority of one classification (7 of 10 excitatory and 19 of 21
1201 excitatory and one cell was approximately split 6 of 11 excitatory). For further analyses, we
1202 separated these three mixed clusters into an excitatory and inhibitory cluster each to yield a total
1203 of 31 AN-stimulation clusters.
1204
1205 *Calcium Imaging*
1206 After acquisition of fluorescent signals in cochlear nucleus bushy cells in Atoh7/Math5 Cre;
1207 GCaMP6f wedge slices (see above), fluorescence changes in response to electrical stimulation of
1208 axons were measured to determine the effect of synaptic stimulation of bushy cells with and
1209 without blockers of post-synaptic receptors. Polygonal ROIs were drawn by hand around
1210 neurons and any major processes that could be resolved (Elements software version 4.51.01), and
1211 average intensity values for ROIs were calculated for each frame. Maximum fluorescence
1212 elicited from AN stimulation within a protocol was compared to baseline average (F) of each
1213 ROI. Fluorescence change (ΔF) and relative fluorescence change (ΔF/F) was calculated using
1214 Excel. Heat maps were constructed from the intensity value output of a given frame from the
1215 Elements software using custom MATLAB scripts. Baseline values were calculated as the

1216 average pixel intensity of the first 15 frames (~5 seconds) before axon stimulation. Cells were
1217 considered active if the average fluorescence of an ROI reached two standard deviations (SD)
1218 above the baseline average in at least 2 of the 3 stimulations during a protocol. Active cells were
1219 then used to compare the ΔF/F between control and glutamate block conditions.
1220
1221 *Data analysis and statistics*
1222 Statistical analyses were performed in Origin (v2021 and v2022). Normality tests were
1223 performed on data sets using the Shapiro-Wilk test. The majority of data sets were non-normally
1224 distributed so non-parametric testing was employed. The Mann-Whitney U test was used for
1225 testing between two independent groups. A One-Sample Wilcoxon Signed Rank Test determined
1226 whether E-I latency difference values were significantly different from zero for MdL- and AN-
1227 stimulation PSCs. Action potential metrics collected at different stimulus rates (Figure 6) were
1228 compared in the control condition using Friedman's ANOVA. Post-hoc Dunn's test was used to
1229 test significance between stimulus rates. Action potential metrics were also compared between
1230 control and inhibition block conditions using paired Wilcoxon Signed Rank Test. Calcium
1231 imaging data were analyzed using Kruskal-Wallis ANOVA where post-hoc Dunn's test was used
1232 to test whether control data sets between the CNQX and CNQX+APV conditions were
1233 significantly different from each other. Population data are summarized in box plots with the box
1234 representing the 1st and 3rd quartiles, the line representing the median, the square representing the
1235 mean and the error bars representing the 10th and 90th percentiles. Figures were prepared in
1236 Origin and Adobe Illustrator.
1237
1238

1239 **Supplementary Tables**

1240

	MdL-EPSC	MdL-EPSC n (clusters / cells)	MdL-IPSC	MdL-IPSC n (clusters / cells)	p-value (Mann-Whitney U Test)
Amplitude, -60 mV (pA)	66.95±3.95	25/17	55.39±3.10	21/15	0.69
Rise Time (ms)	0.63±0.19	25/17	0.86±0.15	21/15	8.02E-04
Time constant of decay (τ, ms)	2.23±0.52	23/17	3.51±0.93	21/15	4.95E-07
Latency (ms)	1.92±0.37	18/18	4.47±0.93	15/15	4.79E-06

1241

1242 **Table S1.** Parameters of MdL-stimulation-evoked PSCs from Figure 1D, for all clusters.

1243

1244

	ΔF/F	p-value	% suppression from control
control (106)	1.176±0.075		
CNQX	1.059±0.018	1.04E-20	67.67±12.43
CNQX wash	1.150±0.073	2.74E-13	
control (121)	1.160±0.071		
CNQX + APV	1.039±0.009	1.14E-34	74.51±11.31
CNQX + APV wash	1.125±0.055	2.54E-24	

1245

1246 **Table S2**. Top: Fluorescence changes in Atoh7/Math5Cre; GCaMP6f expressing bushy cells in control conditions,
1247 with CNQX, and wash of CNQX. Bottom: Fluorescence changes in control, with CNQX + APV, and wash of
1248 CNQX + APV. Differences between conditions tested with Friedman's ANOVA followed by post-hoc Dunn's Test.
1249 % suppression from control: (control DF/F-block DF/F) / (control DF/F-1)*100%. Number of cells for each set of
1250 experiments in parentheses.
1251

1252

	AN-EPSC	AN-EPSC n (clusters / cells)	AN-IPSC	AN-IPSC n (clusters / cells)	p-value (Mann-Whitney U Test)
Amplitude -60 mV (pA)	60.6±39.0	13/8	25.6±11.1	17/10	0.14
Rise Time (ms)	0.86±0.15	13/8	0.92±0.31	17/10	0.35
Time constant of decay (τ, ms)	2.80±1.65	11/8	3.59±1.50	16/10	0.67
Latency (ms)	5.83±1.22	13/8	6.71±0.87	17/10	0.04

1253
1254 **Table S3**. Parameters of AN-stimulation evoked PSCs from Figure 4E, for all clusters.

1255

1256

1257

	MdL-EPSC (18)	MdL-IPSC (15)	AN-EPSC (8)	AN-IPSC (11)
Latency (ms)	1.92±0.37	4.47±0.93	5.22±0.98	6.19±0.77
Onset Jitter (ms)	0.25±0.13	0.50±0.17	0.37±0.13	0.56±0.11
Probability	0.80±0.19	0.45±0.15	0.24±0.08	0.14±0.06

1258

1259 **Table S4.** Parameters of the first cluster of PSCs evoked from MdL- and AN-stimulation from Figure 5. Numbers in
1260 parentheses indicate number of cells.
1261

1262

Rate	Treatment (n)	AP Prob	AP Rate (Hz)	# stimulations to first AP	Latency to first AP
10 Hz	Control (7)	0	0	>20	>2000
10 Hz	Block (7)	0	0	>20	>2000
10 Hz	Wash (5)	0	0	>20	>2000
50 Hz	Control (7)	0.005±0.005	0.25±0.25	19.0±1.0	379.2±20.9
50 Hz	Block (7)	0.053±0.053	2.63±2.63	7.80±4.40	144.4±86.87
50 Hz	Wash (5)	0	0	>20.0	>400
100 Hz	Control (7)	0.035±0.015	3.49±1.51	14.15±4.30	139±44.6 #
100 Hz	Block (7)	0.078±0.036 *	7.78±3.75 *	5.40±2.76 *	49.8±29.1 *
100 Hz	Wash (5)	0.051±0.03	5.08±3.00	9.50±5.13	126±56.7
200 Hz	Control (7)	0.045±0.040 #	9.00±8.00 #	14.2±4.20 #	69.3±22.3 #
200 Hz	Block (7)	0.075±0.047 *	15.0±9.40 *	6.00±2.00 *	26.3±12.0 *
200 Hz	Wash (5)	0.013±0.013	2.67±2.67	16.6±3.50	75.7±19.5

1263

1264 **Table S5.** Measurements of AP probability, rate, the number of stimulations to first AP, and latency to first AP in 5-
1265 8 MOC neuron recordings in response to MdL-stimulation at the frequency indicated, from Figure 6C. Measurements
1266 are presented in control, during pharmacological blockade of post-synaptic inhibitory receptors ("block"), and wash
1267 conditions, as median±MAD. Numbers in parentheses indicate n. # indicates significantly different from control 10
1268 Hz stimulation (Friedman ANOVA with post-hoc Dunn's test). * indicates significantly different from control within
1269 stimulus frequency comparison (P<0.05, Paired Wilcoxon Signed-Rank Test).
1270

1271